Dalton Transactions

ROYAL SOCIETY OF CHEMISTRY

PERSPECTIVE

View Article Online
View Journal | View Issue

Check for updates

Cite this: *Dalton Trans.*, 2026, **55**, 2766

Red/near-infrared emitting phosphors based on Bi^{3+} ions: recent advances, materials design, and applications

Xuejiao Wang, *[a] Sihan Yang[a] and Ji-Guang Li *[b]

Received 6th October 2025,
Accepted 22nd December 2025

DOI: 10.1039/d5dt02387d

rsc.li/dalton

In recent years, Bi^{3+}-doped luminescent materials have attracted widespread attention due to their diverse electronic transition types and tunable emission properties. While most Bi^{3+}-doped phosphors primarily emit in the ultraviolet to yellow spectral region, recent studies have successfully achieved efficient broadband red and near-infrared (NIR) emission through strategies such as crystal field/defect engineering and energy transfer, thereby breaking the traditional limitations of the emission spectrum. This review systematically summarizes the latest progress in Bi^{3+}-based red/NIR phosphors, with emphasis on the luminescence mechanism, material design strategy, performance influencing factors, and application prospects in optical thermometry, plant cultivation lighting, and information encryption. Finally, we discuss current challenges and future research directions, aiming to provide theoretical guidance and insights for the development of novel high-performance Bi^{3+}-doped long-wavelength phosphors.

1 Introduction

Phosphors activated by Bi^{3+} ions ([Xe] $4f^{14}5d^{10}6s^2$ electronic configuration) have attracted considerable attention in recent years due to their exceptional luminescence properties.[1–4] The phosphors exhibit diverse emission origins, including isolated ion emission, charge transfer states, and ion-pair interactions, and typically demonstrate broadband emissions spanning from the ultraviolet (UV) to yellow spectral region.[5–9] However, extending the emission spectra to longer wavelengths, particularly in the red and near-infrared (NIR) regions, remains a significant scientific challenge though it may offer several advantages. In contrast to the parity-forbidden f–f transitions of rare-earth ions and the parity-forbidden d–d transitions of transition metal ions, the emission of isolated Bi^{3+} ions is primarily attributed to outer electron transitions between the $6s^2$ ground state ($^1S_0$) and the 6s6p excited states ($^3P_0$, $^3P_1$, $^3P_2$, and $^1P_1$). This fundamental difference gives rise to a unique characteristic spectrum, which includes the famous A band ($^1S_0 \rightarrow {}^3P_1$, parity-allowed and partially spin-forbidden), the B band

---

[a] School of Materials and Environmental Engineering, Bohai University, Jinzhou, Liaoning 121013, China. E-mail: wangxuejiao@bhu.edu.cn; Tel: +86-416-3400708
[b] Research Center for Electronic and Optical Materials, National Institute for Materials Science, Tsukuba, Ibaraki 305-0044, Japan. E-mail: li.jiguang@nims.go.jp; Tel: +81-29-860-4394

Xuejiao Wang

Xuejiao Wang is currently a full professor at Bohai University. She received her Ph D in materials science from Northeastern University (China) in 2017. Her research interests include the luminescence of rare earth/transition metal ions and optically functional ceramic materials.

Sihan Yang

Sihan Yang is currently a Master's degree candidate in materials science and engineering at Bohai University, and her supervisor is Xuejiao Wang. Her research mainly focuses on high-performance rare earth/transition metal luminescent materials.

($^1S_0 \rightarrow {}^3P_2$, parity-allowed and spin-forbidden), and the C band ($^1S_0 \rightarrow {}^1P_1$, both parity and spin-allowed). Compared to the conventional rare-earth (RE) ions for red phosphors (*e.g.*, Eu^{2+} and Sm^{3+}), Bi^{3+} possesses unique merits as a main-group activator, including superior elemental abundance, cost-effectiveness, and environmental benignity. Owing to its exposed 6s electrons, Bi^{3+} shows optical properties sensitive to the local crystal field and exhibits luminescence characteristics strongly dependent on the strength and covalency of the host lattice. By adjusting the composition and local structure of the host material, the luminescence performance of Bi^{3+} can be precisely controlled.[10–13] The characteristic excitation of Bi^{3+}-doped materials occurs in the near-UV/UV region rather than the visible light region, thus effectively avoiding the problem of spectral reabsorption in Eu^{2+}- or Ce^{3+}-activated broadband phosphors. This raises luminescence efficiency and significantly improves the color purity of the pc-WLED devices.[14–16] Furthermore, though Cr^{3+} is a predominant activator for NIR phosphors, the emission intensity of Cr^{3+} is highly dependent on the crystal field strength of its surrounding lattice environment. More critically, Cr^{3+} is prone to form higher-valence ions (Cr^{4+} and Cr^{6+}) under oxidative conditions, which significantly compromises the efficiency of NIR luminescence.[17,18] The inherent limitations of the aforementioned RE^{3+} and Cr^{3+} activators have accelerated the growing demand for developing novel, non-toxic and cost-effective red/NIR-emitting phosphors. In this regard, developing Bi^{3+}-activated novel phosphors and elucidating the underlying mechanisms of Bi^{3+} luminescence hold substantial scientific importance, and the resulting phosphors may also find promising applications in solid-state lighting and agriculture photonics.

Ji-Guang Li

Ji-Guang Li is currently a chief researcher at the National Institute for Materials Science (NIMS) in Japan. He received his Ph D in materials science from the Northeastern University in China in 1998. He conducted research as an STA fellow researcher at the then National Institute for Research in Inorganic Materials (NIRIM) in Japan during 1999–2001 and as a postdoctoral researcher at NIMS during 2001–2002 before being appointed as a staff scientist at NIMS in 2002. He was a visiting scholar at the Georgia Institute of Technology in the USA during 2008–2009.

His research focuses on design, controlled fabrication and evaluation of optically functional inorganic materials. He is currently an Associate Editor of RSC journals Journal of Materials Chemistry C and Materials Advances.

Currently, the research on efficient broadband red/NIR luminescent materials based on Bi^{3+} activation remains limited, and the relationship between spectral characteristics and the local structure of the host matrix has not been fully elucidated. Therefore, mechanistic exploration of the red/NIR luminescence of Bi^{3+} holds significant scientific value. This review systematically summarizes the latest research progress on Bi^{3+}-doped red/NIR phosphors, with a focus on the key factors affecting luminescence performance. It also outlines the strategies and underlying mechanisms of spectral regulation, aiming for precise design of the red/NIR emission involving Bi^{3+}. The materials design approaches discussed herein may also be extended to other luminescent systems. Additionally, this review offers perspectives on the challenges and future directions for the development of Bi^{3+}-based red/NIR phosphors.

2 Spectral characteristics of Bi^{3+}

2.1 Energy level characteristics of Bi^{3+}

As a non-rare-earth luminescent center, the Bi^{3+} ion has been extensively investigated for its unique optical properties. A free Bi^{3+} ion has an $^1S_0$ ground state, with excited states derived from the 6s6p electronic configuration ordered by increasing energy as $^3P_0$, $^3P_1$, $^3P_2$, and $^1P_1$. Fundamentally, investigating the luminescence of ions with an s^2 electronic configuration necessitates careful consideration of their complex excited-state relaxation dynamics. These systems are prone to undergo significant transition state relaxation in the excited state. For lighter s^2 ions, the dominant relaxation mechanism typically involves the Jahn–Teller effect, which lowers the system's energy by distorting the local geometry, thereby breaking orbital degeneracy and inducing energy level splitting. In contrast, for heavier s^2 ions such as Bi^{3+}, strong spin–orbit coupling plays a more critical role. The substantial spin–orbit coupling not only mixes the $^3P_1$ and $^1P_1$ states, enhancing the spin-allowed character of the $^1S_0 \rightarrow {}^3P_1$ transition, but also activates the fully spin-forbidden $^3P_0$ state, granting it spectroscopic activity. Due to its long decay lifetime, the $^3P_0$ state facilitates competitive non-radiative relaxation pathways.[19–22] Among the excitation transitions of Bi^{3+}, $^1S_0 \rightarrow {}^1P_1$ is spin-allowed, $^1S_0 \rightarrow {}^3P_2$ is weakly observable due to occasional coupling with asymmetric lattice vibrational modes, $^1S_0 \rightarrow {}^3P_1$ becomes partially spin-allowed through spin–orbit coupling-induced mixing of the $^3P_1$ and $^1P_1$ states, and $^1S_0 \rightarrow {}^3P_0$ is fully spin-forbidden. The absorption bands of Bi^{3+}-doped materials arising from $^1S_0 \rightarrow {}^3P_1$, $^3P_2$, and $^1P_1$ transitions are conventionally labeled as A, B, and C bands, respectively.[23–26] The $^1S_0 \rightarrow {}^3P_1$ and $^1S_0 \rightarrow {}^1P_1$ transition channels have reasonable absorption intensities, enabling effective excitation and emission in Bi^{3+}-doped phosphors. Remarkably, through rational host engineering, Bi^{3+} can exhibit tunable emission spanning from UV to NIR spectral regions. However, the regulation engineering based on 6s6p intrinsic transition has performance instability. Specifically, when attempting to shift the emission wavelength into the red or even NIR region, the required reduction in the energy gap significantly lowers the energy barrier (activation energy, ΔE) between the excited and ground states. This leads to an exponential increase in the probability of non-radiative transitions, which in turn causes severe thermal quenching and a decrease in efficiency. This inherent drawback makes it difficult to obtain efficient, stable, and long-wavelength luminescence from Bi^{3+} based solely on this approach, thereby motivating researchers to integrate other methods, such as enhancing structural rigidity and defect engineering, to achieve outstanding performance.

Studies have shown that theoretical prediction of the absorption band positions of Bi^{3+}-doped luminescent materials can be achieved by combining dielectric theory with an analysis of the host lattice environment.[27] Wang *et al.* successfully established a quantitative relationship between the absorption positions of the A/C bands and an environmental factor h_e through a systematic analysis of the crystallographic parameters of Bi^{3+}-doped compounds:[27]

$$h_e = \sum[f_c(i)\alpha(i)Q(i)^2]^{\frac{1}{2}} \tag{1}$$

$$E_A = 2.972 + 6.206\ \exp(-h_e/0.551) \tag{2}$$

$$E_C = 3.236 + 10.924\ \exp(-h_e/0.644) \tag{3}$$

where h_e represents the environmental factor; $f_c(i)$ and $\alpha(i)$ refer to the fractional covalency and volume polarization between the central ion and its nearest ligand, respectively; $Q(i)$ denotes the charge carried by the anion; and E_A and E_C represent the energies of the A and C transitions, respectively.

2.2 Charge transfer (CT) transitions

In addition to intra-ion transitions, the optical behavior of Bi^{3+}-activated phosphors also requires consideration of the contributions from extra-ion transitions. In certain Bi^{3+}-doped compounds, the observed absorption and emission bands originate from metal-to-metal charge transfer (MMCT) between Bi^{3+} and the transition metal ions in the host lattice. The excited state is formed by the interaction between the Bi^{3+} energy levels and the metal cation levels, which have a $\mathrm{d}^0/\mathrm{d}^{10}$ electron configuration.[28,29] Based on the energy difference between the MMCT state and the A band transition, three types of luminescence behaviors can be observed (Fig. 1): (a) MMCT-dominant emission when $E(\mathrm{MMCT}) < E(^3\mathrm{P}_{1,0})$; (b) coexisting emission from both MMCT and $^3\mathrm{P}_{1,0}$ states when $E(\mathrm{MMCT}) \approx E(^3\mathrm{P}_{1,0})$; and (c) $^3\mathrm{P}_1 \rightarrow {}^1\mathrm{S}_0$ dominated emission when $E(\mathrm{MMCT}) > E(^3\mathrm{P}_{1,0})$, though MMCT-mediated emission may still occur. The MMCT energy can be estimated using the following empirical formula, which helps to analyze its contribution to the luminescence:[2]

$$\mathrm{MMCT}\,(\mathrm{Bi}^{3+},\ \mathrm{cm}^{-1}) = 70\,000 - 52\,000\frac{\chi_4(\mathrm{M}^{n+})}{d_{\text{corr}}} \tag{4}$$

$$\mathrm{MMCT}\,(\mathrm{Bi}^{3+},\ \mathrm{cm}^{-1}) = 55\,000 - 45\,500\frac{\chi_{\text{CN}'} > 4(\mathrm{M}^{n+})}{d_{\text{corr}}} \tag{5}$$

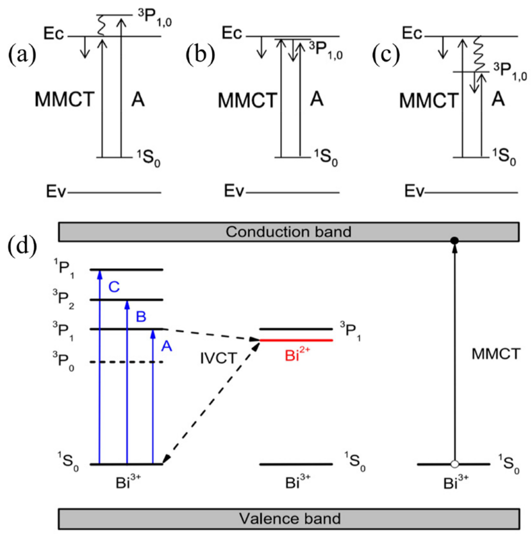

Fig. 1 (a)–(c) Different configurations of the energy levels leading to luminescence in Bi^{3+}-doped solids. Reproduced with permission from ref. 2, copyright 2013, American Chemical Society. (d) The diagram of the inter-configurational electronic transitions, intervalence charge transfer (IVCT) transition and metal-to-metal charge transfer (MMCT) transition of the Bi^{3+} ion. Reproduced with permission from ref. 32, copyright 2016, Elsevier.

$$d_{\text{corr}} = d_{\text{host}} + \frac{1}{2}[r(\mathrm{Bi}^{3+}) - r(\text{host})] \tag{6}$$

Formula (4) is valid for 4-coordinated M^{n+} metals, while formula (5) is valid for metals with a coordination number greater than 4. The optical electronegativity of the transition metal is denoted as $\chi(\mathrm{M}^{n+})$. The corrected shortest distance between Bi^{3+} and M^{n+} is represented by d_{corr}, whereas d_{host} refers to the unadjusted shortest distance between Bi^{3+} and M^{n+}. Additionally, $r(\mathrm{Bi}^{3+})$ and $r(\text{host})$ correspond to the ionic radii of Bi^{3+} and the host cations replaced by Bi^{3+}, respectively. This implies that by strategically designing the matrix to control $E(\mathrm{MMCT})$, the emission wavelength can be directly tuned to the deep red or even NIR region. Furthermore, the MMCT transition is orbital-allowed and thus inherently holds potential for high-intensity luminescence. However, the emission efficiency is highly dependent on whether Bi^{3+} and M^{n+} can form tight ion pairs or clusters within the lattice. If the ion pairs are randomly distributed and far apart, the resulting MMCT emission will be rather weak.

In compounds with high Bi^{3+} doping concentrations, adjacent Bi^{3+} ions (Bi^{3+} pairs) may undergo redox reactions, leading to intervalence charge transfer (IVCT) processes. This phenomenon can be described by the following electronic transition: $\mathrm{Bi}^{3+}\ (6\mathrm{s}^2) + \mathrm{Bi}^{3+}\ (6\mathrm{s}^2) \rightarrow \mathrm{Bi}^{4+}\ (6\mathrm{s}^1) + \mathrm{Bi}^{2+}\ (6\mathrm{s}^2 6\mathrm{p}^1)$. It should be emphasized that such IVCT transitions are thermodynamically feasible only when the ground state energy level of Bi^{2+} lies below the first excited state ($^3\mathrm{P}_1$) of Bi^{3+}, as shown in Fig. 1(d).[3,30,31] Systematic investigations by Dorenbos *et al.*[32] revealed that in most Bi^{3+}-doped materials, in addition to the characteristic A-band emission (typically located in the high-energy region), an additional emission band is frequently observed in the low-energy region. Comprehensive analysis suggests that this emission band originates from IVCT transitions of Bi^{3+} ion pairs. The energy position of these IVCT transitions can be predicted using the following empirical formula:[33]

$$\mathrm{IVCT}\,(\mathrm{Bi}^{3+},\ \mathrm{cm}^{-1}) = K_{\mathrm{CN}}\left[\chi_{\mathrm{CN}}(\mathrm{Bi}^{3+}) - \alpha_{\mathrm{CN}}\frac{\chi_{\mathrm{CN}}(\mathrm{Bi}^{3+})}{d_{\mathrm{corr}}}\right] \tag{7}$$

$$d_{\mathrm{corr}} = d_{\mathrm{host}} + \frac{1}{2}\left[2r(\mathrm{Bi}^{3+}) - r(M) - r(M')\right] \tag{8}$$

where $\chi_{\mathrm{CN}}(\mathrm{Bi}^{3+})$ represents the electronegativity of Bi^{3+} under the coordination number CN and K_{CN} and α_{CN} are parameters related to the Bi^{3+} ion. The term d_{corr} refers to the interatomic distance of the Bi^{3+}–Bi^{3+} pair after doping effects are corrected, while $r(\mathrm{Bi}^{3+})$, $r(M)$, and $r(M')$ represent the ionic radii of the Bi^{3+} ion and the ionic radii of the host cations occupied by two adjacent Bi^{3+} ions, respectively.

3 Broadband red/NIR luminescence based on Bi^{3+} ions

In recent years, Bi^{3+}-based inorganic materials emitting in the near-ultraviolet (n-UV) to yellow light region (300–600 nm) have been extensively developed and proven to play a crucial role in applications such as LEDs, display technologies, and optical sensors. However, the design and realization of Bi^{3+}-activated materials emitting at longer wavelengths, particularly in the red and NIR regions, remain limited, though such materials possess irreplaceable advantages due to their unique optical properties and are highly valuable for both scientific research and practical applications.

3.1 Broadband red luminescence based on Bi^{3+} ions

The tunable emission characteristics of Bi^{3+} stem from the remarkable sensitivity of the $6s^2$ electron configuration to local coordination environments. Kang *et al.*[34] elegantly demonstrated this fundamental mechanism in the $(Y,Lu,Sc)VO_4:Bi^{3+}$ system, where adjusting the ratio of Lu/Y and Sc/Lu induces systematic contraction of Bi–O bond lengths. This structural modification drives a progressive redshift of the emission peak from 435 nm (blue) to 635 nm (red), as shown in Fig. 2(a) and (b). Such a phenomenon can be quantitatively explained by the dielectric chemical bond theory: the reduced bond length enhances the covalency of Bi^{3+}–O^{2-} bonds, which subsequently increases the crystal field splitting energy and ultimately results in an emission redshift. The researchers also established a clear correlation between the emission wavelength of Bi^{3+} and the average covalency (f_c) of Ln–O bonds (Fig. 2(c)), and, through systematic analysis, revealed a positive relationship between the two. Such a principle was further validated in the $(Y,Sc)(Nb,V)O_4:Bi^{3+}$ system, where precise control of V/Nb and Sc/Y atomic ratios enabled continuous tuning of the emission peaks from 456 nm (blue) to 647 nm (red) through bond length engineering, as seen in Fig. 2(d).[35] These findings demonstrate that rational cation substitution can be an effective strategy for tailoring the luminescence properties of Bi^{3+}-doped materials *via* bond length (covalency) modification.

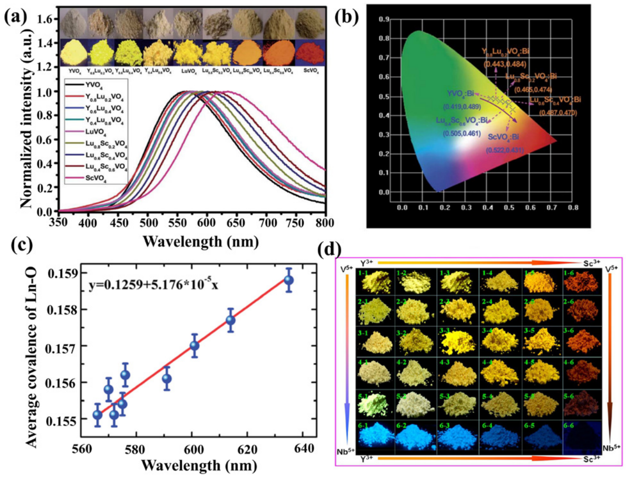

Fig. 2 (a) Emission spectra of solid solution compounds $(Y_x,Lu_y,Sc_z)_{0.98}VO_4:0.02Bi$ (x, y, and z = 0–1.0) under 265 nm excitation; inset: digital photographs of the corresponding samples exposed to natural light (upper) and a UV lamp with a wavelength of 254 nm. (b) CIE chromaticity coordinates. (c) Dependence of the Bi^{3+} emission position on the average Ln–O covalency in the solid solution compounds, where the red line is generated using the equation $y = 0.1259 + 5.176 \times 10^{-5}x$. Reproduced with permission from ref. 34, copyright 2014, Royal Society of Chemistry. (d) Exemplary photographs of Bi^{3+} luminescence in some $(Y,Sc)(Nb,V)O_4:Bi^{3+}$ compounds during exposure to a UV-C lamp. Reproduced with permission from ref. 35, copyright 2016, American Chemical Society.

The enhanced crystal field by bond length changes and lattice distortion is the key factor leading to the red shift of Bi^{3+} emission. Dang *et al.*[36] constructed $Ba_{1+x}Sr_{1-x}Ga_4O_8:Bi^{3+}$ (x = 0–0.7) phosphors using a cation substitution strategy for the $Ba_2Ga_4O_8:Bi^{3+}$ system with a $P6_3(173)$ space group. Systematic investigations revealed that as Sr^{2+} progressively substituted Ba^{2+}, the shortening of bond lengths and the increase in polyhedral distortion index (D) together enhanced the crystal field splitting energy. Additionally, the significant reduction in average electronegativity improved spectral polarization. These effects collectively induced a pronounced redshift in both the characteristic emission bands of two emissive Bi^{3+} centers, enabling precise luminescence tuning from a cyan green (~470 nm) to red (~630 nm) color (Fig. 3(a)–(c)). An analogous emission modulation mechanism has been corroborated in the $(Lu_{0.99-x}Gd_x)_2WO_6:0.01Bi^{3+}$ (x = 0–0.99) system by Wang *et al.*,[37] where green emission at 510 nm dominates when x = 0–0.5 and distinct red emission emerges at 610 nm for x = 0.75–0.99 (Fig. 3(d)). This red shift phenomenon can be attributed to the significant substitution of Gd^{3+}, which enhances $[BiO_8]$ polyhedral distortion (Fig. 3(e) and (f)), crystal field splitting, the covalency of the Bi^{3+}–O^{2-} bond (due to reduced electronegativity difference) and polarization.

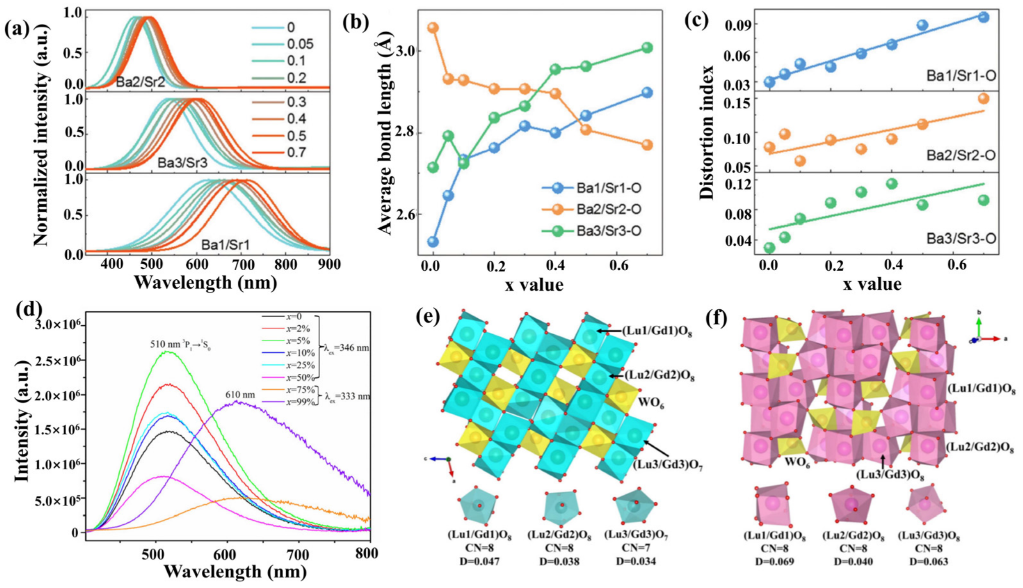

Fig. 3 (a) Normalized Gaussian fitting PL spectra of $Ba_{1+x}Sr_{1-x}Ga_4O_8$:Bi^{3+} (x = 0–0.7) at the three Ba/Sr sites, (b) average bond lengths of Ba_1/Sr_1–O, Ba_2/Sr_2–O and Ba_3/Sr_3–O, (c) polyhedron distortion indices of Ba_1/Sr_1, Ba_2/Sr_2 and Ba_3/Sr_3. Reproduced with permission from ref. 36, copyright 2020, Royal Society of Chemistry. (d) The PL spectra of $(Lu_{0.99-x}Gd_xBi_{0.01})_2WO_6$ (x = 0–0.99). The crystal structures and the calculated polyhedral distortion index of $(Lu_{0.99-x}Gd_xBi_{0.01})_2WO_6$ for (e) x = 0–0.25 and (f) x = 0.75–0.99. Reproduced with permission from ref. 37, copyright 2023, Royal Society of Chemistry.

Chen *et al.*[38] presented a novel design strategy for Bi^{3+}-based red-emitting phosphors. Through Gaussian fitting of the emission spectrum of $NaLaScNbO_6$:Bi^{3+},Li^+, they revealed the synergistic contribution from the A-type transition, Bi^{3+}–Nb^{3+} MMCT, and matrix oxygen vacancy luminescence, as shown in Fig. 4(a), where the dominant orange-red emission at 625 nm is primarily due to MMCT-induced emission, as predicted by empirical formulas. Moreover, this study demonstrates that modulating the degree of lattice order–disorder can significantly influence luminescence properties. The

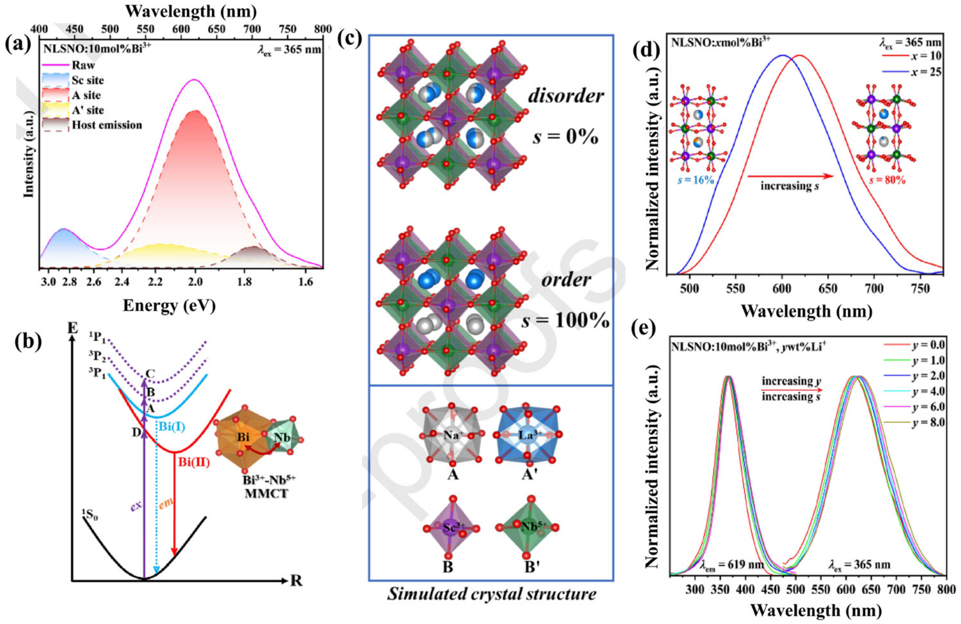

Fig. 4 (a) The Gaussian fitting peaks of $NaLaScNbO_6$:Bi^{3+} (NLSNO:Bi^{3+}). (b) Energy level scheme of Bi^{3+} ions. (c) Simulated crystal structure of NLSNO within A-site disordered and ordered models. (d) The PL spectra of the A-site disordered and ordered models. (e) Normalized PL and PLE spectra of NLSNO:10 mol%Bi^{3+},$y$$Li^+$ (y = 0–8 wt%). Reproduced with permission from ref. 38, copyright 2024, Elsevier.

primary distinction between the ordered and disordered structures lies in the arrangement of A-site cations (Fig. 4(c)): in the ordered model, Na^+ and La^{3+} (or Bi^{3+}) occupy distinct crystallographic sites in a layered configuration, whereas in the disordered model, these cations are randomly distributed over the A and A′ sites without long-range order. The A-site ordering degree (s) can be evaluated using the formula $s = (2\omega_A - 1) \times 100\%$, where ω_A represents the occupancy of A-site cations at their expected positions. As the doping content x decreases from 25 mol% to 10 mol%, the calculated s increases from 16% to 80%. Upon further addition of 6 wt% Li_2CO_3 flux, the s continues to rise to 99%. This trend can be attributed to the fact that in the standard double perovskite structure, the larger A′ site is more suitable for accommodating high-charge trivalent cations such as La^{3+} or Bi^{3+}. However, as the Bi^{3+} doping concentration increases, the electrostatic repulsion between Bi^{3+} and La^{3+} becomes more pronounced. As a result, at x = 25 mol%, a higher proportion of Bi^{3+} ions tend to occupy the A site rather than the A′ site, thereby reducing the overall ordering degree. Furthermore, the introduction of flux helps to reduce structural defects and further enhance cationic ordering. In summary, by adjusting the contents of Bi^{3+} activators and flux additive, the extent of lattice ordering can be effectively tuned. As shown in Fig. 4(c) and (d), when the s increases from 16% to 80%, the emission red shifts from 599 nm to 619 nm. Further increasing the s from 80% (partially ordered) to 99% (nearly completely ordered) *via* Li^+ co-doping also results in the expected redshift. This redshift is attributed to the enhanced structural rigidity (higher Debye temperature Θ_D) and weaker electron–phonon coupling in the ordered structure, which collectively contribute to improved thermal stability, prolonged luminescence lifetime, and higher quantum efficiency of the phosphor. This work not only systematically elucidates the luminescence mechanism of Bi^{3+}-based red-emitting phosphors but also provides valuable theoretical insights and experimental guidance for performance optimization.

3.2 Broadband NIR luminescence based on Bi^{3+} ions

Broadband NIR luminescent materials hold significant application value and development potential in diverse fields, including medical physiotherapy, security monitoring, bioimaging, and food quality analysis. Among various NIR-emitting materials, Bi^{3+} ions have emerged as superior activators due to their remarkable properties, including efficient UV/NUV excitation, high luminescence efficiency, non-reabsorption characteristics, and excellent luminescence performance in pc-LED devices.

$BaAl_{12}O_{19}$, a highly symmetric host material with the $P6_3/mmc$ space group, features a unique crystal structure that provides diverse polyhedral coordination environments including MO_9 (M = Ba1, Ba2), MO_6 (M = Al1, Al4), and MO_4 (M = Al2, Al3, Al5). This creates favorable conditions for Bi^{3+} ions to exhibit diverse photoluminescence properties. Wei *et al.*[39] successfully achieved tunable luminescence (blue to NIR region) in $BaAl_{12}O_{19}:Bi^{3+}$ by precisely controlling the synthesis atmosphere. It was found that the emission tuning primarily stems from oxygen vacancy (V_o)-induced selective site occupation of Bi^{3+} (Fig. 5(a)): under a N_2/H_2 reducing atmosphere, a high concentration of V_o promotes preferential occupation of Bi^{3+} at higher-coordination number Ba^{2+} sites, leading to deep-blue emission at 440 nm, and in contrast, the material has fewer

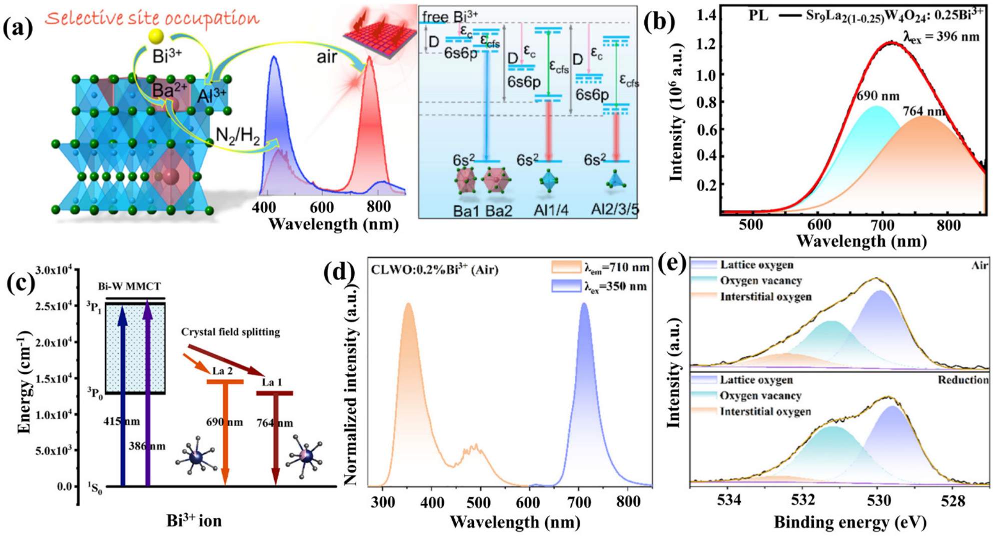

Fig. 5 (a) NIR emission in Bi^{3+}-doped highly symmetric $BaAl_{11}O_{19}$, and a schematic diagram of the movement of the Bi^{3+} 6s6p energy level at various cationic sites. Reproduced with permission from ref. 39, copyright 2020, American Chemical Society. (b) Gaussian fitting of the PL spectrum of the $Sr_9La_2W_4O_{24}:0.25Bi^{3+}$ phosphor under 396 nm excitation. (c) Energy level diagram and luminescence mechanism of $Sr_9La_2W_4O_{24}:Bi^{3+}$. Reproduced with permission from ref. 40, copyright 2025, Elsevier. (d) The normalized excitation and emission spectra of the $Ca_3La_2W_2O_{12}:0.2\%Bi^{3+}$ phosphor. (e) O-1s XPS spectra of the $Ca_3La_2W_2O_{12}$ phosphors synthesized under air and reducing atmosphere. Reproduced with permission from ref. 41, copyright 2024, Elsevier.

oxygen vacancies when synthesized in air, which causes Bi^{3+} to predominantly occupy lower-coordination number sites, such as MO_6 octahedra or MO_4 tetrahedra, resulting in NIR luminescence. This study offers novel insights for the development of Bi^{3+}-activated NIR phosphors through an in-depth understanding of the mechanism of the NIR luminescence of Bi^{3+}. The $Sr_9La_2W_4O_{24}$:Bi^{3+} phosphor, on the other hand, exhibits luminescence covering the wavelength range of 550–850 nm under 396 nm excitation, which closely matches the absorption spectra of phytochromes P_R and P_{FR}, suggesting its potential application in plant growth lighting. As shown in Fig. 5(b), the emission profile can be deconvoluted into two Gaussian components centered at 690 nm and 764 nm, which are attributed to Bi^{3+} ions occupying the La_2 and La_1 sites in the crystal lattice, respectively. Further calculations indicated that higher bond covalency is responsible for the NIR emission of Bi^{3+}, consistent with the linear relationship between bond covalency (f_c) and emission wavelength depicted in Fig. 2(c).[40] For another special case, the $Ca_3La_2W_2O_{12}$:Bi^{3+} phosphor, reported by Qin *et al.*,[41] emits NIR light centered at 710 nm under 350 nm excitation, which originates from the self-activated luminescence of the matrix. Comparative experiments on the sintering atmosphere serve as an effective approach for investigating such self-activated luminescence. The results indicate that the sample prepared under a reducing atmosphere exhibits a significant decrease in NIR emission intensity compared to the one sintered in air, suggesting that the luminescence mechanism may be related to oxygen-associated defects. Further high-resolution XPS analysis of the O1s orbital reveals a notable reduction in the fitted peak area corresponding to interstitial oxygen under the reducing atmosphere. This trend aligns with the decrease in NIR luminescence intensity, confirming that interstitial oxygen defects are the key origin of the self-activated NIR emission. Upon Bi^{3+} doping, the Bi^{3+} ions would occupy the $[LaO_6]$ sites, which creates atomic disorder and lattice distortion and thus enhances the formation probability of interstitial oxygen in the lattice (Fig. 5(d) and (e)). Combining a self-activated NIR emitting matrix with a Bi^{3+} activator to enhance NIR luminescence properties may therefore provide a new strategy for further development. In addition to the above examples, Table 1 summarizes the latest research advancements on Bi^{3+}-doped broadband red/NIR emitting phosphors, along with the crystal structure and photoluminescence (PL) properties.

4 Design strategies for Bi^{3+}-based red/NIR luminescence

In this section, we will focus on the design strategy of Bi^{3+} -based red/NIR luminescent materials, aiming to provide a clearer understanding of the material design logic (Fig. 6).

4.1 Crystal field engineering

4.1.1 Selection of matrix materials. The electronic transitions of Bi^{3+} are highly sensitive to the local coordination environment. The physical origin of the emission redshift lies in the fact that in environments with strong crystal fields and high bond covalency, the energy of the excited state ($^3P_1$) is significantly reduced to a much greater extent than that of the ground state ($^1S_0$). In other words, the excited state ($^3P_1$) of Bi^{3+} becomes substantially more stabilized relative to the ground

Table 1 Crystal structure and PL parameters of Bi^{3+}-doped red/NIR phosphors

Compounds	Space group	λ_{ex} (nm)	λ_{em} (nm)	FWHM (nm)	QE (%)	I@T (°C)	Ref.
$ScVO_4$	$I4_1/amd$	265/330	635	128	35	86%@150	34, 42 and 43
$Y_{0.2}Sc_{0.8}VO_4$	$I4_1/amd$	330	621	225.9	49.4	—	35
$Ba_{1.5}Sr_{0.5}Ga_4O_8$	$P6_3(173)$	325	630	283	—	97.1%@150	36
Gd_2WO_6	$C2/c$	333	610	220	4.09	—	37
$NaLaScNbO_6$	$C2/m$	370	625	123	76	50%@150	38
$BaAl_{12}O_{19}$	$P6_3/mmc(194)$	332	770	82	—	—	39
$Sr_9La_2W_4O_{24}$	$I4_1/a$	396	714	170	52.87	~15%@150	40
$Ca_3La_2W_2O_{12}$	$R\bar{3}m$	350	710	36	48.82	69.09%@150	41
$Na_2Ca_3Nb_2O_9$	$R3_2$	365	667	215	84.2	37%@150	44
$Sr_3BiY_3B_4O_{15}$	$P6_3(173)$	257	605	~200	98.1	~60%@125	45
Zn_2SiO_4	$R\bar{3}$	310	750	104	33	67%@150	46
$LaSr_2SbO_6$	$P12_1/n1$	370	600	108	—	71%@150	47
La_4GeO_8	$P1$	397	600	103	88.3	78.4%@125	48
$ZnWO_4$	$P12/c1(13)$	365	665	~225	—	—	49
$BaGa_2O_4$	$P6_3$	325	638	~150	75.1	88.1%@200	50
K_2MgGeO_4	$Pca2_1(29)$	335	614	148	66	72%@150	51
Gd_2MoO_6	$C2/c$	362	670	~250	—	—	52
$Y_2Ti_2O_7$	$Fd\bar{3}m$	391	744	120	—	—	53
$Ba_2Ga_2GeO_7$	$P\bar{4}2_1m(113)$	400–420	611	~125	—	—	54
$SrBaZn_2Ga_2O_7$	$P6_3mc$	338	600	~200	16	~35%@150	55
$Cs_2Ag_{0.6}Na_{0.4}InCl_6$	$Fm\bar{3}m$	365	610	171	84	~50%@125	56
$Ba_3WO_5Cl_2$	$Cmcm$	471	708	—	—	—	57
$Sr_3Ga_4O_9$	$P\bar{1}$	380	680	~150	—	—	58
$Sr_{0.6}La_{1.4}ZnO_{4.2}$	$I4/mmm$	390	609	130	13	~10%@150	59
$SrSc_2O_4$	$Pnam$	298	711	—	34	110%@150	60

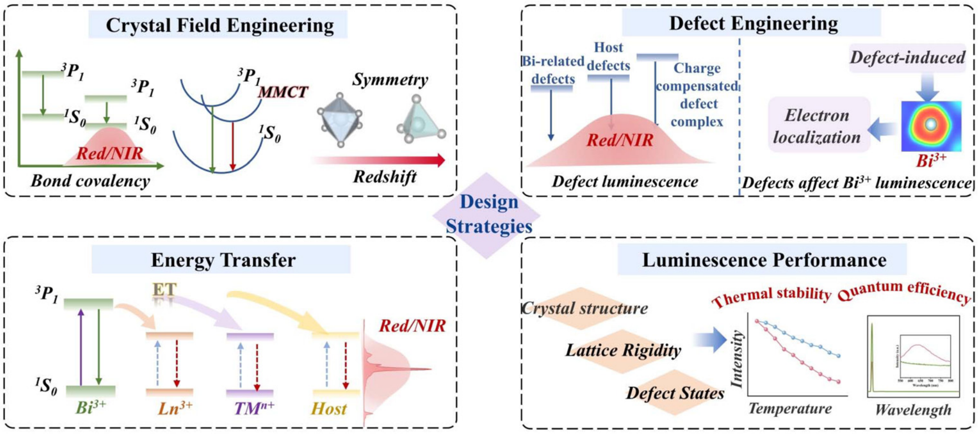

Fig. 6 Schematic illustration of the design strategies for Bi^{3+}-based red/NIR luminescence.

state ($^1S_0$), resulting in a narrowing of the energy gap for the $^3P_1 \rightarrow {}^1S_0$ transition. This reduced energy gap leads to a redshift in the emission wavelength. Therefore, the luminescence properties of Bi^{3+} are closely correlated with the crystal structure of the host material, and selecting an appropriate host is essential to achieve emission within the desired wavelength region.

Li *et al.*[61] conducted a systematic study on the luminescent behavior of $Ca_5(BO_3)_3F$:Bi^{3+} and found that the emission redshift is primarily due to an enhanced nephelauxetic effect and increased crystal field splitting. In this system, Bi^{3+} exists in three different coordination environments, with covalent strength following the order $Ca_2O_6 > Ca_1O_5F > Ca_3O_4F_2$ due to the differences in ligand electronegativity. With increasing concentration, Bi^{3+} ions preferentially occupy the Ca_3 site, followed by gradual substitution at Ca_1 and Ca_2 sites. This results in a decrease in average ligand electronegativity, an increase in bond covalency, enhanced nephelauxetic effects and a downward shift of the energy centroid, ultimately causing a redshift in the emission spectrum. Concurrently, the average distance between Bi^{3+} ions decreases with increasing concentration, which strengthens interionic interactions and further elevates the strength of the local crystal field. Moreover, as the ligand environment shifts from mixed O^{2-}/F^- to pure O^{2-} coordination, crystal field splitting energy (Δ) increases, intensifying the splitting of the $^3P_1$ energy level and promoting a further shift of the emission spectrum toward longer wavelengths (Fig. 7(a) and (b)). Although this system did not achieve tunable red emission, the underlying mechanism provided valuable theoretical guidance for future materials design. Regarding host selection, prioritizing compounds containing highly polarizable anions (*e.g.*, $Se^{2-} > S^{2-} > I^-$) is an effective strategy. The central mechanism is that the higher the polarizability of the anion, the stronger the covalency of the chemical bond formed with Bi^{3+}. This enhances the overlap between the electron clouds of the Bi^{3+} 6s/6p orbitals and the anion p orbitals, significantly lowering the energy of the Bi^{3+} 6p orbital, ultimately leading to a redshift in the emission spectrum. However, reports systematically considering the impact of anion polarizability in material design remain relatively limited. A compelling example is the typical CaS:Bi^{3+} phosphor, which emits blue light at room temperature. When the S^{2-} in the matrix is replaced by more polarizable Se^{2-}, the resulting CaSe:Bi^{3+} exhibits a significant redshift of its emission to 645 nm.[62]

Additionally, high-valent transition metal ions with a d^0 electron configuration (*e.g.*, Mo^{6+}, W^{6+}, and V^{5+}) can form metal–metal charge transfer (MMCT) states with Bi^{3+} and are therefore emerging as a family of ideal candidates for matrix components. Previous studies have shown that low-energy MMCT states can effectively contribute to red emission, as exemplified by the Bi^{3+}–Nb^{5+} MMCT transition in $Na_2Ca_3Nb_2O_9$:Bi^{3+} and the Bi^{3+}–Y^{3+} MMCT process responsible for the 605 nm emission in $Sr_3Y_3B_4O_{15}$:Bi^{3+}.[44,45] Even within the same matrix, the lower the symmetry of the Bi^{3+}-occupied lattice site, the more pronounced the crystal field splitting effect, which is favorable for the luminescence redshift. In Zn_2SiO_4:Bi^{3+}, for example, Li *et al.*[46] speculated that the NIR emission originates from the Bi^{3+} occupying the lower-symmetry tetragonal ring site rather than the hexagonal ring site, as shown in the crystal structure in Fig. 7(c). In the luminescence spectrum of $MgGa_2O_4$:Bi^{3+},[63] the blue emission centered at 430 nm is attributed to the Bi^{3+} occupying octahedral sites (GaO_6/MgO_6) while the NIR emission at 709 nm originates from the Bi^{3+} residing in tetrahedral sites (GaO_4/MgO_4) (Fig. 7(d)). Similarly, in the aforementioned $BaAl_{11}O_{19}$:Bi^{3+} system,[39] a decrease in oxygen vacancy concentration induces Bi^{3+} to occupy lower symmetry sites, thereby producing NIR emission.

4.1.2 Cation substitution. Ion substitution has been widely employed to modulate the local crystal field environment of Bi^{3+}. This strategy involves replacing the cationic species in the host matrix with other cations of different ionic radii and identical or different valence states, thereby altering the coordination structure around Bi^{3+} and consequently inducing spectral shifts.

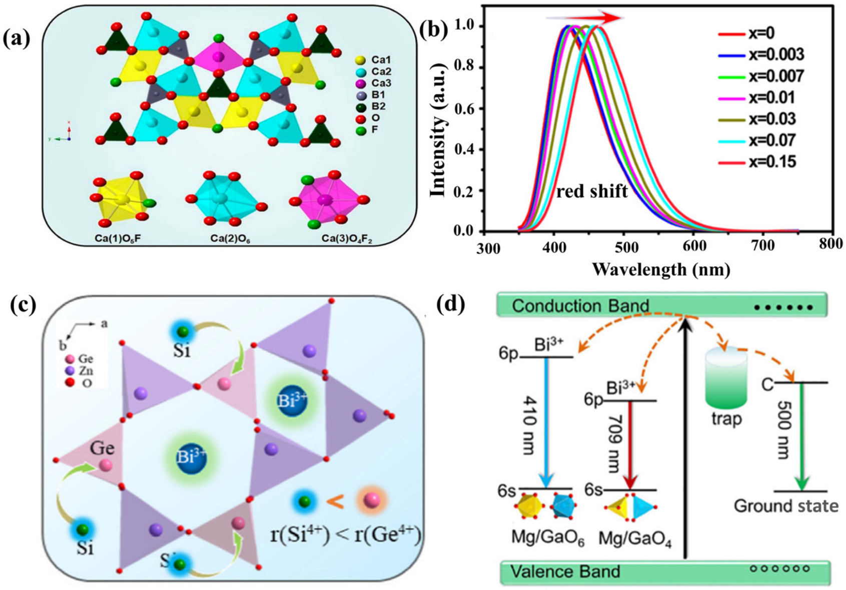

Fig. 7 (a) Crystal structure of Ca$_5$(BO$_3$)$_3$F and the coordination environment of Ca$_1$, Ca$_2$, and Ca$_3$. (b) Normalized emission spectra of Ca$_5$(BO$_3$)$_3$F : xBi^{3+} (x = 0, 0.003, 0.007, 0.1, 0.3, 0.7, 0.15) under 322 nm excitation. Reproduced with permission from ref. 61, copyright 2017, American Chemical Society. (c) Local luminescence diagram of Zn$_2$(Ge/Si)O$_4$:Bi^{3+}. Reproduced with permission from ref. 46, copyright 2023, Elsevier. (d) A schematic diagram of the mechanism of MgGa$_2$O$_4$:Bi^{3+} luminescence. Reproduced with permission from ref. 63, copyright 2022, Elsevier.

In general, the host lattice consists of coordination polyhedra formed by cations and anions, wherein the cations can be classified into two types: host cations (C$_h$) and cations within the anion coordination polyhedra (C$_{ic}$). Cationic substitution serves as an effective approach for tuning the luminescence properties of phosphors. Substitutions can occur at C$_h$ sites, such as alkaline earth ions (Mg^{2+}, Ca^{2+}, Sr^{2+}, and Ba^{2+}), alkali ions (Li$^+$, Na$^+$, and K$^+$), and rare-earth ions (Y^{3+}, Sc^{3+}, La^{3+}, Gd^{3+}, and Lu^{3+}) and can also occur at C$_{ic}$ sites, as exemplified by the Nb^{5+} in (NbO$_4$)$^{3-}$, V^{5+} in (VO$_4$)$^{3-}$, and P^{5+} in (PO$_4$)$^{3-}$. Taking the representative (Y$_{1-y}$Sc$_y$)(Nb$_{1-x}$V$_x$)O$_4$:Bi^{3+} system as an example,[35] tunable luminescence from blue to orange and even deep red can be achieved through ion substitution. This phenomenon is attributed to the reduced bond length of Bi^{3+}–O^{2-} and the enhanced crystal field strength during substitution, which collectively lead to a redshift in the emission spectrum. Similarly, in the zircon-type ScPO$_4$ host doped with Bi^{3+}, partial substitution of P^{5+}–O^{2-} with V^{5+}–O^{2-} significantly increases the covalency of the chemical bonds and the strength of the crystal field around Bi^{3+} ions, resulting in a shift of the emission wavelength from 455 nm to 641 nm, as shown in Fig. 8(a) and (b).[64] Moreover, a recent study revealed that, under 370 nm excitation, the LaSr$_2$SbO$_6$:Bi^{3+} phosphor exhibits broadband orange-red emission centered at around 600 nm, whose spectral position and intensity can be tuned *via* Si^{4+} → Sb^{5+} cationic substitution and [Si^{4+}–Zn^{2+}] → [Sr^{2+}–Sb^{5+}] cationic-pair substitution (Fig. 8(c) and (d)). The underlying mechanism involves heterovalent substitution, which introduces Si$_{Sb}$ defects into the structure. This enhances the electron localization around Bi^{3+} ions and strengthens the crystal field, leading to changes in luminescence intensity and a red shift of 43 nm in the emission position.[47]

4.2 Defect engineering

The core concept of the defect engineering strategy for achieving red and NIR emission from Bi^{3+} involves introducing intrinsic or extrinsic defects into the host lattice to construct specific defect energy levels. These defects interact with Bi^{3+} ions, thereby modulating the luminescence behavior and enabling emission tuning from UV/blue to red and even NIR wavelengths. The role of oxygen vacancies in inducing electron localization around Bi^{3+} ions, leading to highly efficient orange-red emission, was demonstrated by Li *et al.* in the development of La$_4$GeO$_8$:Bi^{3+} phosphors (Fig. 9(a) and (b)).[48] The incorporation of Bi^{3+} ions causes slight changes in the local lattice coordination environment of the La$_4$GeO$_8$ host, thereby facilitating the formation of oxygen vacancies. DFT calculations were performed to compare the electronic structures of Bi^{3+} occupying La$_1$–La$_3$ sites with and without oxygen vacancy defects. The results reveal that the electron transition energy levels associated with Bi-6p orbitals appear between the valence and conduction bands only in the presence of oxygen vacancies, which confirms that oxygen vacancy defects are essential for generating orange-red luminescence in La$_4$GeO$_8$:Bi^{3+}. Further ELF analysis indicates that the oxygen vacancies promote electron localization around Bi^{3+}, which is conducive to efficient long-wavelength emission. This strategy offers new perspectives and insights for diverse luminescence regulation. In the case of ZnWO$_4$:Bi^{3+}, Han *et al.*[49] demonstrated that the tunable emission from blue to red is intrinsically governed by

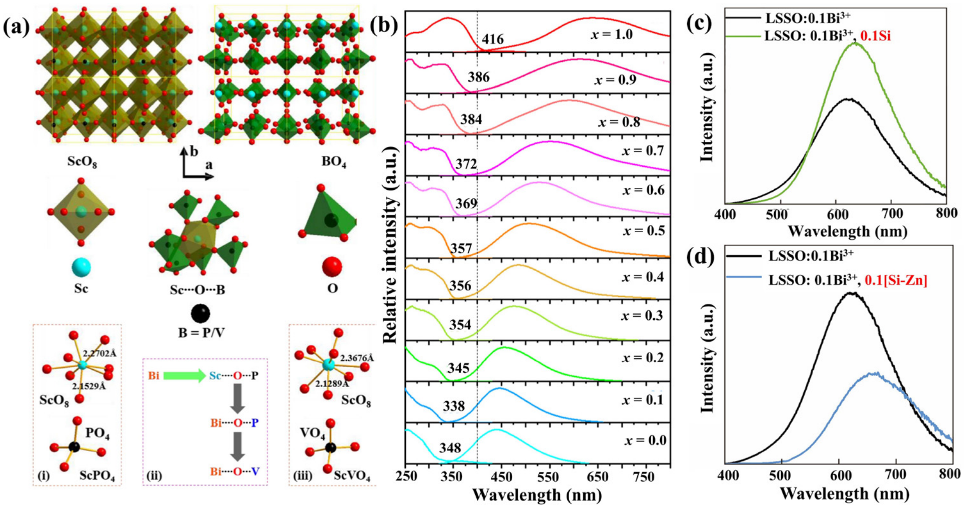

Fig. 8 (a) Crystal structures of ScVO$_4$ and ScPO$_4$. (b) Normalized excitation and emission spectra of Sc(V$_x$P$_{1-x}$)O$_4$:Bi^{3+} ($0 < x < 1$) solid solutions. Reproduced with permission from ref. 64, copyright 2019, Royal Society of Chemistry. (c) Emission spectra of LaSr$_2$SbO$_6$:Bi^{3+} and LaSr$_2$SbO$_6$:Bi^{3+}, Si^{4+} (λ_{ex} = 370 nm). (d) Emission spectra of LaSr$_2$SbO$_6$:Bi^{3+} and LaSr$_2$SbO$_6$:Bi^{3+},Si^{4+},Zn^{2+} (λ_{ex} = 370 nm). Reproduced with permission from ref. 47, copyright 2025, Chinese Academy of Sciences.

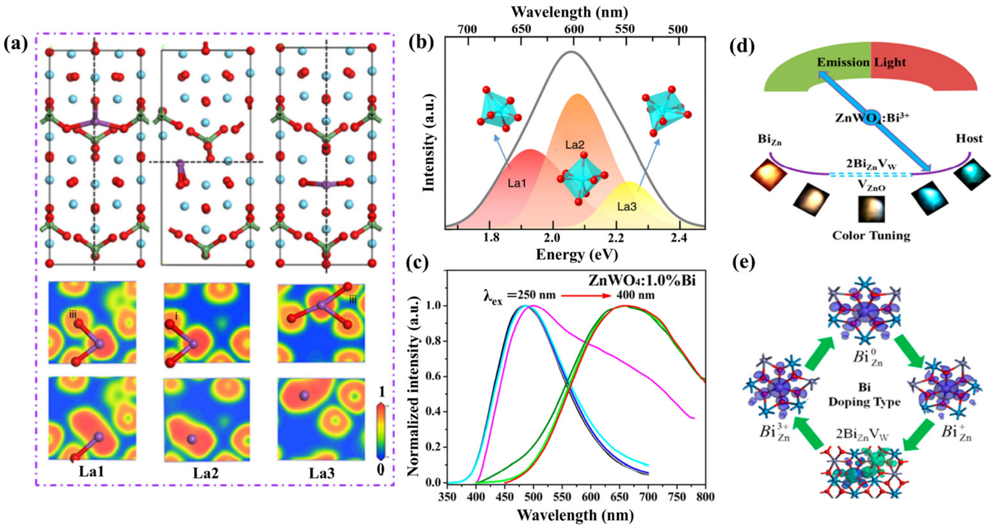

Fig. 9 (a) Structural configuration for Bi^{3+}-doping into three La^{3+} sites of La$_4$GeO$_8$ and the electron localization function (ELF) maps without (up) and with (down) oxygen vacancies in the three La sites. (b) Gaussian fitting peaks of the representative La$_4$GeO$_8$:0.007Bi^{3+} sample. Reproduced with permission from ref. 48, copyright 2019, Nature Publishing Group. (c) Emission spectra of ZnWO$_4$:Bi^{3+} under different excitation wavelengths from 250 to 400 nm. (d) Schematic diagram of tunable luminescence in ZnWO$_4$:Bi^{3+}, with the images of tunable emission being demonstrated in the lower row. (e) Transition between different types of defects such as Bi$_{Zn}{}^{0}$, Bi$_{Zn}{}^{+}$, and Bi$_{Zn}{}^{3+}$, and charge-compensated complex 2Bi$_{Zn}$V$_W$. Reproduced with permission from ref. 49, copyright 2017, American Chemical Society.

the formation of specific Bi-related defects (Fig. 9(c)). DFT calculations revealed that under oxidizing synthesis conditions, substituting Zn^{2+} with Bi^{3+} (denoted as Bi$_{Zn}{}^{3+}$) is the most energetically favorable process due to its markedly lower formation energy compared to other defects. This preference makes Bi$_{Zn}{}^{3+}$ the primary and stable source of the observed ~665 nm red emission. However, the introduction of a trivalent cation (Bi^{3+}) into a divalent site (Zn^{2+}) creates a local charge imbalance. To maintain charge neutrality, the system spontaneously forms charge-compensated defect complexes. The most probable complex is [2Bi$_{Zn}{}^{3+}$·V$_W{}^{6-}$], where two Bi$_{Zn}{}^{3+}$ defects are coupled with a single W-site vacancy (V$_W$) that carries an effective negative charge. This specific charge compensation mechanism is crucial for stabilizing the Bi dopants in the lattice and enriches the defect ecosystem. The resulting diversity of defects—including the dominant Bi$_{Zn}{}^{3+}$, the charge-compensated complexes, and intrinsic vacancies—creates a spectrum of discrete energy levels within the bandgap. It is the selective excitation of these specific defects, each with its own characteristic transition energy, that enables the wide-range emission tuning. As the excitation wavelength shifts from 250 nm (host absorption) to 400 nm (defect-related absorption), different defects are activated, leading to the observed gradual redshift in emission from 498 nm to 672 nm (Fig. 9(d) and (e)).

4.3 Energy transfer engineering

In Bi^{3+}-based red/NIR phosphors, designing efficient energy transfer pathways from the Bi^{3+} sensitizer to specific activators (*e.g.*, Eu^{3+}, Mn^{4+}, Sm^{3+}, *etc.*) is a crucial approach for achieving high-efficiency luminescence. This strategy leverages the strong UV/NUV absorption of Bi^{3+} to compensate for the inherently weak absorption of most red/NIR emitting centers. The energy transfer process allows for flexible tuning of the relative intensity of the dual emissions by simply adjusting the relative doping concentrations of Bi^{3+} and the activator, and accordingly has been widely adopted in the development of color-tunable single-phase phosphors. The occurrence of energy transfer requires two fundamental conditions: first, there must be a significant spectral overlap between the emission spectrum of the sensitizer and the excitation spectrum of the activator to ensure energy matching; second, a suitable interaction mechanism—electric multipole interaction or exchange interaction—must exist between the two types of ions. To experimentally verify the energy transfer process, the following approaches are commonly employed: (1) exciting the phosphor at the optimal excitation wavelength of the sensitizer to observe the characteristic emission of the activator, and (2) monitoring the fluorescence lifetime of the sensitizer, where a systematic decrease in lifetime with increasing activator content can further confirm the presence of non-radiative energy transfer. Consequently, deliberate design of the energy transfer pathway is crucial for the rational development of Bi^{3+}-based red/NIR phosphors.

4.3.1 $Bi^{3+} \rightarrow Ln^{3+}$ energy transfer. Eu^{3+} is a well-known red-emitting activator, whose luminescence originates from its $^5D_0 \rightarrow {}^7F_J$ (J = 0–4) transitions. Among these, the $^5D_0 \rightarrow {}^7F_2$ transition (around 615 nm) is a forced electric dipole transition that produces intense red emission with high color purity. In the $CaYGaO_4$:Bi^{3+},Eu^{3+} system,[65] Wang *et al.* successfully constructed an efficient pathway for $Bi^{3+} \rightarrow Eu^{3+}$ energy transfer. By modulating the concentration of Eu^{3+}, the emission color could be continuously tuned from the blue emission of Bi^{3+} to the orange-red emission dominated by Eu^{3+} (Fig. 10(a)–(c)). Moreover, the thus-prepared materials exhibit promising performance as single-component phosphors for application in pc-WLEDs, as shown in Fig. 10(d). Similarly, in the $Sr_2Ta_2O_7$:Bi^{3+} system, Bi^{3+} exhibits broadband blue emission centered at 475 nm due to the MMCT effect. By introducing Eu^{3+} or Sm^{3+} as energy acceptors and precisely controlling their concentrations, an effective $Bi^{3+} \rightarrow Ln^{3+}$ (Ln = Eu^{3+}, Sm^{3+}) energy transfer pathway can be established. As the concentration of Ln^{3+} increases, the characteristic red emission of Ln^{3+} significantly gains intensity, enabling continuous modulation of the luminescence color from blue to red. This strategy not only demonstrates the versatility of Bi^{3+} as a sensitizer in regulating red emission but also provides an effective approach for designing novel color-tunable phosphors (Fig. 10(e)–(h)).[66] Nd^{3+} exhibits characteristic emissions at approximately 900 nm ($^4F_{3/2} \rightarrow {}^4I_{9/2}$ transition), 1070 nm ($^4F_{3/2} \rightarrow {}^4I_{11/2}$), and 1330 nm ($^4F_{3/2} \rightarrow {}^4I_{13/2}$), covering both the NIR-I and NIR-II biological windows. Due to the spectral overlap between the excitation bands of Nd^{3+} and the emission profile of Bi^{3+}, efficient energy transfer from Bi^{3+} to Nd^{3+} can be achieved. This has been demonstrated in host lattices such as La_2GeO_5 and $Sr_9La_2W_4O_{24}$, where co-doping Bi^{3+} with Nd^{3+} ions enables efficient NIR emissions, particularly in the NIR-II region.[40,67] Furthermore, other Ln^{3+} ions such as Yb^{3+} and Er^{3+} can also serve as effective acceptors for the energy absorbed by Bi^{3+}, facilitating highly efficient NIR luminescence. This mechanism is of great significance for developing novel NIR pc-LEDs with applications in bioimaging, food quality inspection, and beyond. Representative phosphor systems based on such a mechanism may include $Cs_2AgInCl_6$:Bi^{3+},Er^{3+}/Bi^{3+},Yb^{3+}, Y_2O_3:Bi^{3+},Yb^{3+},Bi^{3+}/Yb^{3+} co-doped gadolinium tungstate, and ZnB_2O_4:Bi^{3+},Er^{3+}, among others.[68–71]

4.3.2 $Bi^{3+} \rightarrow TM^{n+}$ energy transfer. Transition metal (TM) ions such as Mn^{4+}, Cr^{3+}, and Fe^{3+} possess incompletely filled d-orbitals and have d^n electronic configurations ($0 < n < 10$). They serve as important luminescent activators, capable of emitting light across a broad spectral range from the visible to NIR region. The Mn^{4+} ion, owing to its unique $3d^3$ electronic configuration, can undergo efficient $^2E_e \rightarrow {}^4A_{2e}$ transition in an octahedral crystal field to emit deep red lights of 650–680 nm. Constructing a $Bi^{3+} \rightarrow Mn^{4+}$ energy transfer system in a suitable host matrix not only leverages the strong absorption of Bi^{3+} in the UV/n-UV region but also enables high-performance red emission. For the Ba_2GdNbO_6:Bi^{3+},Mn^{4+} phosphor, systematic luminescence tuning from blue to red can be achieved under 315 nm UV excitation, demonstrating promising potential for application in warm pc-WLED lighting (Fig. 11(a) and (b)).[72] The luminescence color of Mn^{2+} can vary from green to deep red depending on the crystal field environment. In general, Mn^{2+} in octahedral coordination tends to emit red light. Moreover, the overlap between the absorption band of Mn^{2+} and the emission band of Bi^{3+} suggests that efficient energy transfer from Bi^{3+} to Mn^{2+} can take place. When Bi^{3+} and Mn^{2+} are co-doped into a CaZnOS host, a characteristic cyan emission at 490 nm from the $^3P_{1,0} \rightarrow {}^1S_0$ transition of Bi^{3+}, a red emission at 616 nm by the $^4T_1(^4G) \rightarrow {}^6A_1(^6S)$ transition of Mn^{2+}, and a greenish emission at 520 nm associated with defect centers can be observed.[73] By adjusting the content ratio of Bi^{3+} and Mn^{2+}, the relative intensity of the green and red emissions can be modulated (Fig. 11(c) and (d)). Furthermore, under cyclic application and release of pressure, the material exhibits mechanoluminescence (ML) color changes from red, orange, and white to cyan, as shown in Fig. 11(e) and (f). This behavior is related to the types of traps present in the lattice, with shallow traps being more favorable for red emission from Mn^{2+}. The above study also demon-

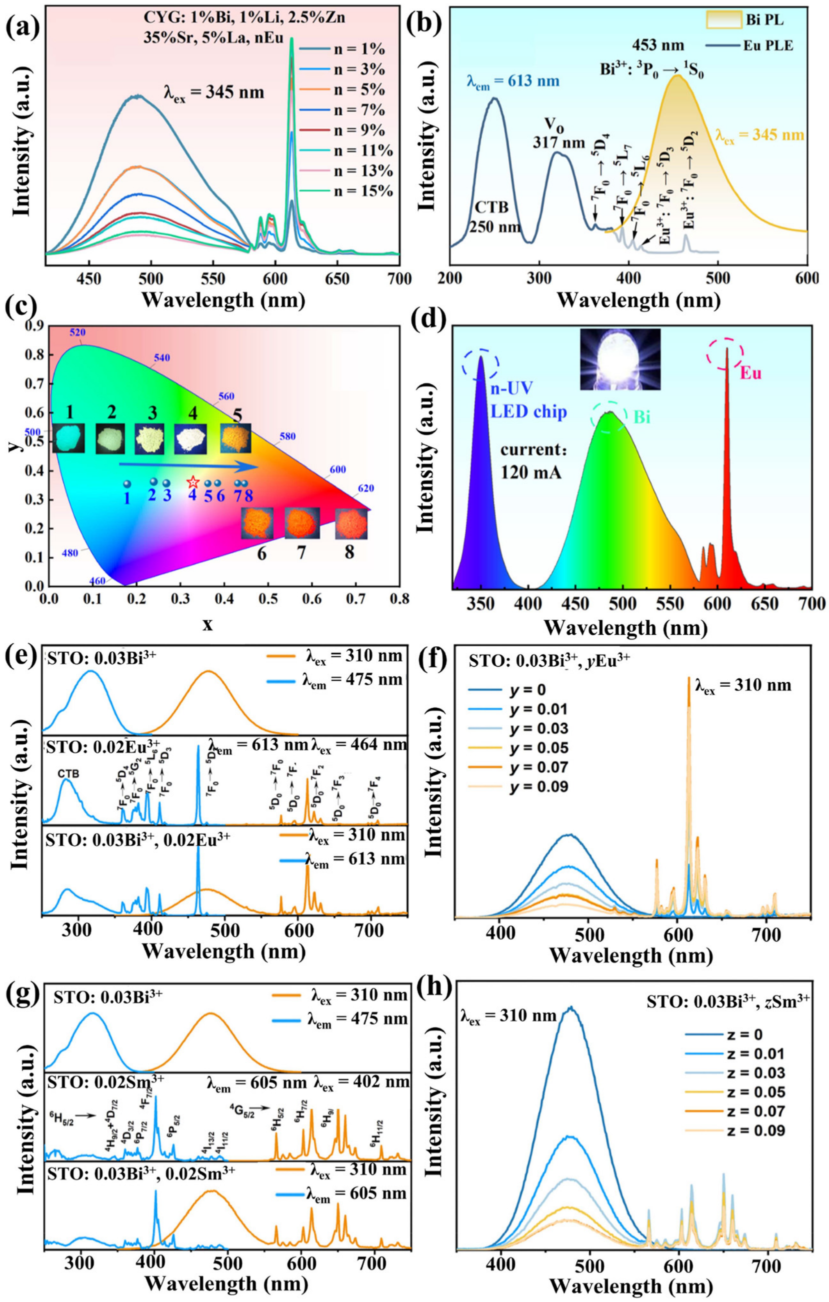

Fig. 10 (a) PL spectra of the $CaYGaO_4$:1%Bi,1%Li,2.5%Zn,35%Sr,5%La,nEu phosphors. (b) The PLE spectrum of Eu^{3+} and PL spectrum of Bi^{3+} in $CaYGaO_4$. (c) CIE coordinates of the phosphors with different doping contents of Eu^{3+}. (d) EL spectra of the device under a 120 mA driving current. Reproduced with permission from ref. 65, copyright 2024, American Chemical Society. (e) PL and PLE spectra of $Sr_2Ta_2O_7:Bi^{3+}$, $Sr_2Ta_2O_7:Eu^{3+}$ and $Sr_2Ta_2O_7:Bi^{3+},Eu^{3+}$. (f) PL spectra of $Sr_2Ta_2O_7:0.03Bi^{3+},yEu^{3+}$. (g) PL and PLE spectra of $Sr_2Ta_2O_7:Bi^{3+}$, $Sr_2Ta_2O_7:Sm^{3+}$, and $Sr_2Ta_2O_7:Bi^{3+},Sm^{3+}$. (h) PL spectra of $Sr_2Ta_2O_7:0.03Bi^{3+},ySm^{3+}$. Reproduced with permission from ref. 66, copyright 2025, Royal Society of Chemistry.

strated promising potential for the application of the phosphor in novel mechanical stress induced displays, ultrasound monitoring, and particularly advanced anti-counterfeiting technologies.[73] It is widely acknowledged that the luminescence properties of Cr^{3+} are highly dependent on crystal field strength, and the efficient red to NIR emission with tunable spectral characteristics of Cr^{3+} has attracted extensive research interest. Systematic studies have thus been conducted on energy transfer systems involving Bi^{3+} and Cr^{3+}. Such phosphors, under UV excitation, may show outstanding luminescence performances by adjusting the concentration ratio of the two ions, such as the modulable intensity ratio of the characteristic emissions of Bi^{3+} and Cr^{3+}, adjustable overall intensity of the NIR emission, high quantum efficiency (QE) of luminescence and so forth. For instance, the $Sr_3Y_2Ge_3O_{12}:Bi^{3+}$, Cr^{3+} phosphor achieved a QE as high as 81.5% and $Gd_3Ca_5O_{12}$:

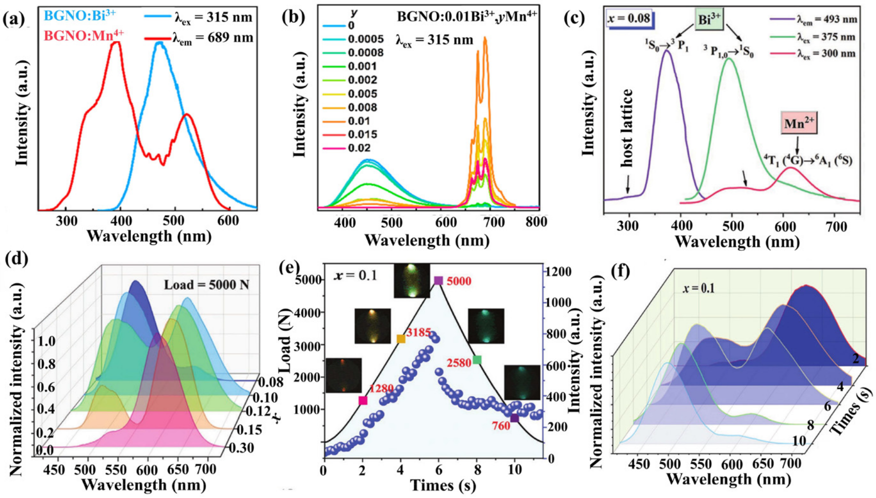

Fig. 11 (a) PLE spectrum of Ba_2GdNbO_6(BGNO):Mn^{4+} and PL spectrum of BGNO:Bi^{3+}. (b) PL spectrum of BGNO:Bi^{3+},Mn^{4+}. Reproduced with permission from ref. 72, copyright 2019, American Chemical Society. (c) The excitation and emission spectra of the CaZnOS:Bi^{3+},Mn^{2+} phosphor exhibiting mechanoluminescence (ML). (d) Normalized ML spectra. (e) ML intensity as a function of pressure during a cycle of pressurization and release, where the insets show the optical images of an epoxy resin–phosphor composite under different pressures. (f) Normalized ML spectra with increasing time. Reproduced with permission from ref. 73, copyright 2021, Wiley-VCH.

Bi^{3+},Cr^{3+} exhibited anti-thermal quenching in the NIR region ($I_{423\ K}/I_{298\ K}$ = 102%).[74,75] These remarkable properties make such phosphors highly promising for applications in pc-LEDs, plant cultivation lighting, optical thermometry, and other related fields.

4.3.3 Bi^{3+} → host energy transfer. In certain self-activated tungstate and molybdate host matrices doped with Bi^{3+}, energy can be transferred from Bi^{3+} to energy levels associated with the $[WO_6]^{6-}$ or $[MoO_6]^{6-}$ groups. Radiative transitions from these levels often occur in the long wavelength region, resulting in red or even NIR emission. For instance, in the typical self-activated $NaLaMgWO_6$ phosphor, the $[WO_6]^{6-}$ group emits NIR light at around 698 nm due to O^{2-}–W^{6+} charge transfer transitions. When Bi^{3+} is introduced as a sensitizer, energy transfer from Bi^{3+} to $[WO_6]^{6-}$ takes place, significantly enhancing the intensity of this NIR emission (Fig. 12(a) and (b)).[76] Similarly, Gd_2MoO_6 acts as a self-activated luminescent material owing to its O^{2-}–Mo^{6+} charge transfer transition, which produces broad-band red emission centered at 670 nm. After doping with Bi^{3+}, Gaussian fitting and empirical formula calculations confirmed that both the MMCT transition between Bi^{3+} and Mo^{6+} and the A-band transition of Bi^{3+} contribute to luminescence.[52] Moreover, highly efficient Bi^{3+} → $[MoO_6]^{6-}$ energy transfer further enhances the emission in the red spectral region (Fig. 12(c)).[52] Table 2 summarizes various systems of Bi^{3+}-based red/NIR phosphors enabled by energy transfer.

5 Key factors affecting the performance of Bi^{3+}-doped red/NIR luminescent materials

As summarized in Table 1, Bi^{3+}-based phosphors exhibit significant variations in key performance metrics, such as quantum efficiency (QE) and thermal stability. These differences are not arbitrary but are intrinsically determined by

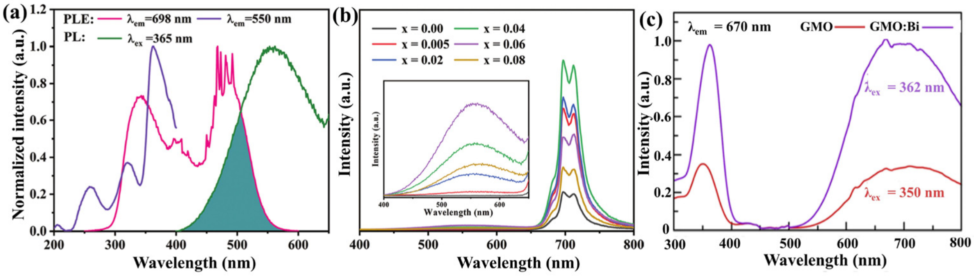

Fig. 12 (a) Normalized excitation and emission spectra of the $NaLaMgWO_6$:Bi^{3+} phosphor, (b) emission spectra of the $NaLa_{1-x}MgWO_6$:xBi^{3+} phosphors. Reproduced with permission from ref. 76, copyright 2022, Wiley-VCH. (c) PL and PLE spectra of Gd_2MoO_6 and Gd_2MoO_6:Bi nanophosphors at 77 K in the visible region. Reproduced with permission from ref. 52, copyright 2024, American Chemical Society.

Table 2 A summary of Bi^{3+}-based red/NIR phosphors through energy transfer

		Sensitizer		Activator		
Sensitizer–activator	Host	λ_{ex} (nm)	λ_{em} (nm)	λ_{ex} (nm)	λ_{em} (nm)	Ref.
Bi^{3+}–Eu^{3+}	$CaYGaO_4$	345	400–600 $^{3}P_{0}$–$^{1}S_{0}$	200–500 $^{7}F_{0}$–$^{5}D_{2-4}$,$^{5}L_{6-7}$	613	65
	$Sr_2Ta_2O_7$:Bi^{3+}	310	350–600 MMCT	250–500 $^{7}F_{0}$–$^{5}D_{2-4}$,$^{5}L_{6}$	613	66
	$NaLaCaWO_6$	376	400–750 $^{3}P_{1}$–$^{1}S_{0}$	200–550 $^{7}F_{0}$–$^{5}D_{2-4}$,$^{5}L_{6-7}$	616	77
	$Ba_3Y_4O_9$	346	350–650 $^{3}P_{1}$–$^{1}S_{0}$	200–550 $^{7}F_{0}$–$^{5}D_{1-2}$,$^{5}L_{6-7}$	617	78
	$BaSc_2O_4$	317	350–600 $^{3}P_{1}$–$^{1}S_{0}$	200–500 $^{7}F_{0}$–$^{5}D_{2}$,$^{5}L_{6-7}$	617	79
	$(Ba,Sr)_3Sc_4O_9$	333	350–750 $^{3}P_{1}$–$^{1}S_{0}$	200–500 $^{7}F_{0}$–$^{5}D_{2}$,$^{5}L_{6-7}$	614	80
	Y_2SiO_5	360	400–650 $^{3}P_{1}$–$^{1}S_{0}$	275–550 $^{7}F_{0}$–$^{5}D_{2-4}$,$^{5}L_{6}$	611	81
	$Ba_2Gd_2Ge_4O_{13}$	291	300–550 $^{3}P_{1}$–$^{1}S_{0}$	200–450 $^{7}F_{0}$–$^{5}D_{2-4}$,$^{5}L_{6-7}$	614	82
Bi^{3+}–Sm^{3+}	$Sr_2Ta_2O_7$:Bi^{3+}	310	350–600 MMCT	350–450 $^{6}H_{5/2}$–$^{4}F_{7/2}$	650	66
Bi^{3+}–Nd^{3+}	La_2GeO_5	316	350–650 $^{3}P_{1}$–$^{1}S_{0}$	200–900 $^{4}I_{9/2}$–$^{2}G_{7/2}$ + $^{2}G_{5/2}$	1058	83
	YVO_4	335	400–700 MMCT	250–650 $^{4}I_{9/2}$–$^{2}G_{7/2}$ + $^{2}G_{5/2}$	880	84
	$Sr_9La_2W_4O_{24}$	396	500–860 $^{3}P_{1}$–$^{1}S_{0}$	200–800 $^{4}I_{9/2}$–$^{2}G_{7/2}$ + $^{2}G_{5/2}$	1070	40
Bi^{3+}–Er^{3+}	$Cs_2AgInCl_6$	370	400–800 $^{3}P_{1}$–$^{1}S_{0}$	250–700 $^{4}I_{15/2}$–$4G_{11/2}$,$^{4}F_{7/2}$, $^{2}H_{11/2}$,$^{4}S_{3/2}$	1540	68
	ZnB_2O_4	335	360–550 $^{3}P_{1}$–$^{1}S_{0}$	375–600 $^{4}I_{15/2}$–$^{4}G_{11/2}$,$^{4}F_{3-9/2}$, $^{4}S_{3/2}$	1535	71
Bi^{3+}–Yb^{3+}	Y_2O_3	378/346	390–600 $^{3}P_{1}$–$^{1}S_{0}$	$^{2}F_{7/2}$–$^{2}F_{5/2}$	976	69
	Gd_2MoO_6	362	450–800 $^{3}P_{1}$–$^{1}S_{0}$, MMCT	300–600 $^{2}F_{7/2}$–$^{2}F_{5/2}$	975	52
Bi^{3+}–Mn^{4+}	Ba_2GdNbO_6	315	350–600 $^{3}P_{1}$–$^{1}S_{0}$	250–600 $^{4}A_{2}$–$^{4}T_{I}$, $^{2}T_{2}$,$^{4}T_{2}$	689	72
	$Ca_3Al_4ZnO_{10}$	340	370–600 $^{3}P_{1}$–$^{1}S_{0}$	240–600 $^{4}A_{2}$–$^{4}T_{I}$, $^{2}T_{2}$,$^{4}T_{2}$	715	85
	$CaSrLaSbO_6$	322	350–500 $^{3}P_{1}$–$^{1}S_{0}$	250–600 $^{4}A_{2}$–$^{4}T_{I}$, $^{2}T_{2}$,$^{4}T_{2}$	678	86
Bi^{3+}–Mn^{2+}	CaZnOS	375	400–650 $^{3}P_{1,0}$–$^{1}S_{0}$	400–600 $^{6}A_{1}$–$^{4}A_{1}$,^{4}E,$^{4}T_{1}$,$^{4}T_{2}$	616	87
	$Y_3Ga_5O_{12}$	330	350–650 $^{3}P_{1}$,$^{1}P_{1}$–$^{1}S_{0}$	400–600 $^{6}A_{1}$–$^{4}A_{1}$,^{4}E,$^{4}T_{1}$,$^{4}T_{2}$	613	88
	$KMgF_3$	300	350–600 $^{3}P_{1}$–$^{1}S_{0}$	250–550 $^{6}A_{1}$–$^{4}A_{1}$,^{4}E,$^{4}T_{1}$,$^{4}T_{2}$	650	89
Bi^{3+}–Cr^{3+}	$Gd_3Ga_5O_{12}$	291	400–660 $^{3}P_{1}$–$^{1}S_{0}$	200–660 $^{4}A_{2}$–$^{4}T_{1}$,$^{4}T_{2}$	724	75
	$Sr_3Y_2Ge_3O_{12}$	370	400–600 $^{3}P_{1}$–$^{1}S_{0}$	250–700 $^{4}A_{2}$–$^{4}T_{1}$,$^{4}T_{2}$	782	74

their microstructural and electronic characteristics. This subsection aims to establish a unified analytical framework to systematically elucidate the core factors governing these properties.

5.1 Structure–property relationship

As previously discussed, enhancing bond covalency facilitates a red-shift in the Bi^{3+} emission but concurrently narrows the emission energy gap. According to the energy gap law, the non-radiative transition rate increases exponentially with the decrease in the energy gap. Consequently, highly covalent systems designed for red/NIR emission often face an inherent constraint on their achievable QE. Nevertheless, a profound understanding of the structure–property relationship can guide performance improvements. A notable example is the $Sr_3BiY_3B_4O_{15}$ phosphor with a fully occupied Bi^{3+} site. Upon 257 nm excitation, it exhibits ultra-broadband emission centered at 605 nm, originating from the combined effects of the $^{3}P_{1}$ excited state and Bi^{3+}–Y^{3+} MMCT. Remarkably, this phosphor achieves a QE as high as 90%, surpassing most broadband red-emitting phosphors. Structural analysis reveals that its unique triangular pore structure provides a stable coordination environment for Bi^{3+} and maintains a maximum Bi–Bi interatomic distance, thereby effectively suppressing concentration quenching caused by cascade energy transfer between activator ions (Fig. 13(a) and (b)).[45]

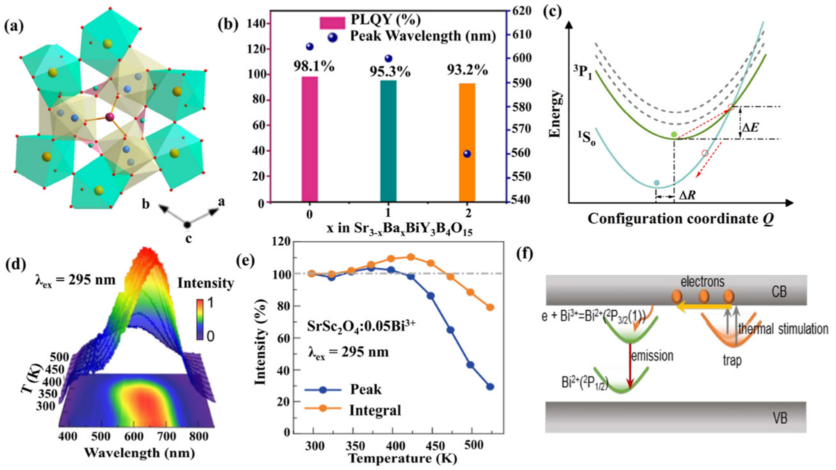

Fig. 13 (a) Schematic crystal structure of the SBYBO phosphor, (b) the photoluminescence quantum yield and peak position diagram of $Sr_{3-x}Ba_xBiY_3B_4O_{15}$ (x = 0, 1, and 2). Reproduced with permission from ref. 45, copyright 2024, American Chemical Society. (c) Thermal quenching mechanisms of Bi^{3+} ions. (d) Temperature-dependent emission spectra of $SrSc_2O_4$:0.05Bi (λ_{ex} = 295 nm), (e) integrated and peak intensity variations of $SrSc_2O_4$:0.05Bi in the region of 298–523 K, and (f) the schematic diagram of the zero-thermal-quenching mechanism. Reproduced with permission from ref. 60, copyright 2022, American Chemical Society.

Furthermore, modulating the degree of lattice order–disorder presents a viable strategy for achieving the target emission wavelength while maintaining high performance. Enhancing cationic ordering within the lattice can increase structural rigidity and reduce electron–phonon coupling. This effect enables the simultaneous realization of an emission redshift and an enhanced QE, reconciling these two seemingly contradictory parameters.[38]

Thermal stability is another critical aspect in evaluating the overall performance of phosphors. For Bi^{3+}, thermal stability is closely related to cross-relaxation between the $^3P_1$ excited state and the $^1S_0$ ground state, as well as thermal ionization at elevated temperatures. Generally, a larger energy difference between the $^3P_1$ level and the cross-relaxation point corresponds to a lower probability of cross-relaxation and better thermal stability; this energy difference can be evaluated using the activation energy (ΔE) (Fig. 13(c)). Simultaneously, a larger energy gap between the $^3P_1$ level and the conduction band bottom reduces the likelihood of thermal ionization, thereby more effectively suppressing thermal quenching and minimizing non-radiative transitions.[90] A comparative study by Zhang *et al.*[44] on the $Na_2Ca_3(Nb,Ta)_2O_9:Bi^{3+}$ system provides clear evidence. Compared to the Ta-containing analogue, $Na_2Ca_3Nb_2O_9:Bi^{3+}$ possesses a narrower band gap and a more red-shifted emission, but exhibits inferior thermal stability. This difference can be attributed to the variations in ΔE between the two samples.

5.2 Lattice rigidity

Lattice rigidity is a fundamental factor determining the performance of luminescent materials. A rigid lattice is characterized by low phonon energy and weak electron–phonon coupling, which effectively suppress phonon-assisted non-radiative transitions. Consequently, high lattice rigidity is a crucial prerequisite for achieving high QE. Furthermore, a rigid lattice provides the structural foundation for a high activation energy (ΔE), making it difficult for excited electrons to overcome the energy barrier *via* thermal perturbation. It also helps to suppress lattice vibrations that can lead to thermal ionization. The lattice rigidity of the host matrix is closely related to the thermal quenching behavior of the activator ions. A framework with high structural rigidity can significantly suppress lattice vibrations at elevated temperatures, thereby reducing the associated emission loss. The Debye temperature (θ_D), obtained through experimental measurements or DFT calculations, serves as a key parameter for evaluating the rigidity of a crystal structure. A higher θ_D generally corresponds to lower lattice vibration frequencies and a smaller Stokes shift, which typically reduces the probability of non-radiative transitions. Therefore, the θ_D is a valuable guiding parameter for screening and identifying host materials with superior thermal quenching resistance. The θ_D can be obtained from the quasi-harmonic Debye model:[91,92]

$$\theta_D = \frac{h}{k_B}\left(6\pi^2 V^{1/2} n\right)^{1/3} f(\sigma)\sqrt{\frac{B_S}{M}} \tag{9}$$

$$f(\sigma) = \left\{3\left[2\left(\frac{2}{3}\frac{1+\sigma}{1-2\sigma}\right)^{3/2} + \left(\frac{1}{3}\frac{1+\sigma}{1-\sigma}\right)^{3/2}\right]^{-1}\right\}^{1/3} \tag{10}$$

where k_B and h represent the simplified Boltzmann constant and Planck constant, respectively; M represents the relative molecular mass of the primitive cell; B_s is the thermal insulator elastic modulus of the crystal; n is the number of atoms present in each primitive cell; V represents the volume of the primitive cell; and σ is the Poisson's ratio. A representative example is the $Ba_{1+x}Sr_{1-x}Ga_4O_8:Bi^{3+}$ (x = 0–0.7) system. The gradual substitution of Sr^{2+} with Ba^{2+} leads to a systematic reduction in thermal quenching, which is directly attributable to the enhanced structural rigidity of the solid solution. This case clearly demonstrates the critical role of lattice rigidity in thermal stability.[36]

5.3 Defect states

Defects are among the key factors influencing the thermal quenching performance of phosphors, and their role is dual-sided, requiring a balanced perspective.

On one hand, appropriately introduced defect energy levels can provide energetic compensation to the luminescent centers during heating, thereby enhancing the anti-thermal quenching performance. A prominent example is the deep red phosphor $SrSc_2O_4:Bi^{3+}$.[60] Its emission originates from a photo-induced charge transfer process: NUV excitation induces electron transfer from a $Bi_{Sc}{}^{3+}$ site to an adjacent $Bi_{Sr}{}^{3+}$ site, forming a $Bi_{Sr}{}^{2+}$ excited state, which subsequently produces deep red emission. This material exhibits an exceptional zero-thermal-quenching behavior, with the emission intensity at 423 K remaining at 110% of its value at 298 K (Fig. 13(d) and (e)). XPS analysis of the O1s orbitals and thermoluminescence (TL) spectroscopy confirmed that this phenomenon is due to defect levels introduced by Bi^{3+}, which capture electrons and reversely compensate the deep red luminescence of Bi ion pairs under thermal stimulation, as shown in Fig. 13(f). Similarly, the red phosphor $BaGa_2O_4:0.02Bi^{3+}$, reported by Li *et al.*,[50] retains about 88.1% of its room-temperature emission intensity at 200 °C. The excellent thermal stability is also attributed to an energy transfer mechanism from trap levels to the luminescent centers. When Bi^{3+} substitutes for Ba^{2+}, it creates effective positive charges $[Bi_{Ba}]$ and an equivalent concentration of negative effective charge. Additionally, intrinsic negative charge defects such as interstitial oxygen $[O_I]$, cation vacancies $[V_{Ba}$ and $V_{Ga}]$, and others are formed during sintering. Under UV excitation, these defect levels trap and store charge carriers. As the temperature increases, the trapped carriers are gradually released from the traps and transferred to the excited state energy levels of the luminescent ions, thereby compensating for the intensity loss due to thermal quenching.

On the other hand, due to the difficulty in precisely controlling the types and concentrations of defects introduced during synthesis, certain defects may become energy loss centers, aggravating non-radiative transitions. Moreover, an excessively high defect concentration can compromise the integrity of the host lattice, reducing the structural stability and ultimately impairing the thermal stability of Bi^{3+}. Consequently, in specific systems such as $LaSr_2SbO_6:Bi^{3+}$, researchers have successfully enhanced the thermal stability by employing flux agents to improve crystallinity and reduce surface defects.[47]

6 Application of the Bi^{3+}-based phosphors

This section will focus on several emerging applications of Bi^{3+}-based red and NIR phosphors, including optical thermometry, plant growth lighting, and anti-counterfeiting and information encryption.

6.1 Optical thermometry

Certain long-wavelength emissions related to Bi^{3+} exhibit high sensitivity to temperature, manifesting as significant and systematic changes in the fluorescence intensity ratio (FIR) or fluorescence lifetime with temperature. In some of these material systems, two independent luminescent centers exist, such as Bi^{3+} occupying different crystallographic sites or Bi^{3+} coexisting with specific defect centers. Due to their distinct thermal response behaviors, the ratio of emission intensities at two selected wavelengths can be monitored to achieve high precision and self-referenced temperature sensing. For instance, $Ba_{1.5}Sr_{0.5}Ga_4O_8:Bi^{3+}$ generates an ultra-wide emission ranging from 350 to 900 nm, with a full width at half maximum (FWHM) of 283 nm, under 325 nm UV excitation, as reported by Dang *et al.*[36] This material contains multiple luminescent centers corresponding to different occupancies of Bi^{3+} at various Sr/Ba sites, each with different temperature dependence of emission. Owing to these characteristics, the material was successfully developed as an optical thermometer for temperature sensing with its I_{477}/I_{627} FIR, achieving a notable relative sensitivity of 1.295% K^{-1} at 100 K, which confirms its promising potential for low-temperature sensing applications (Fig. 14(a)–(d)).

6.2 Plant cultivation lighting

Modern precision agriculture relies on artificial light sources to regulate crop growth and development. Four key pigments

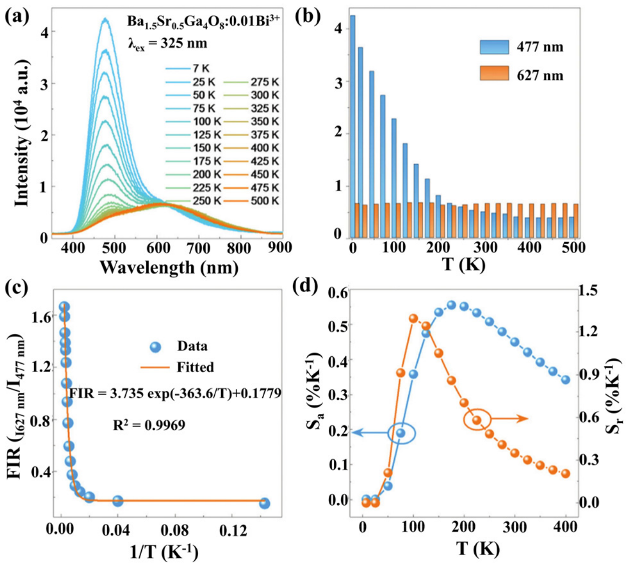

Fig. 14 (a) PL spectra of the $Ba_{1.5}Sr_{0.5}Ga_4O_8:Bi^{3+}$ phosphor at different temperatures (7–500 K). (b) Histogram of intensity for the 477 and 627 nm emissions at various temperatures. (c) FIR(I_{624}/I_{477}) at various temperatures and the fitting result. (d) Dependence of S_a and S_r on temperature. Reproduced with permission from ref. 36, copyright 2020, Royal Society of Chemistry.

in plants, including chlorophyll A, chlorophyll B, red phytochrome (P_R), and far-red phytochrome (P_{FR}), absorb light energy across different spectral regions, collectively regulating photosynthesis and photomorphogenesis. By utilizing phosphors with emission spectra that closely match the absorption spectra of these pigments, precise customization of plant lighting LED sources can be achieved.

Zhang *et al.*[44] developed a UV excitable $Na_2Ca_3Nb_2O_9$:Bi^{3+} red-emitting phosphor, which was integrated with a BAM:Eu^{2+} commercial blue phosphor and a 370 nm UV LED chip to fabricate a plant growth LED device. The emitted light of the device nearly fully covers the primary absorption ranges of both chlorophylls and phytochromes. The output power gradually increases from 19.43 mW at 50 mA to 101.8 mW at 400 mA without saturation, and the photoelectric conversion efficiency reaches its maximum value of 11.3% at a current of 50 mA, demonstrating superior spectral matching performance and photoelectric performance of the LED device (Fig. 15(a)). Similarly, red and NIR phosphors utilizing Bi^{3+}-mediated energy transfer also show significant potential in plant cultivation lighting. For example, in the Gd_2MgTiO_6:Bi^{3+},Cr^{3+} phosphor, efficient $Bi^{3+} \rightarrow Cr^{3+}$ energy transfer enables the material to emit both the blue light of Bi^{3+} and the far-red to NIR light of Cr^{3+} under UV excitation, thereby matching the absorption requirements of both chlorophylls and phytochromes (Fig. 15(b)).[93] Such phosphors can be used to construct spectrally precise LED light sources that promote photosynthesis, control flowering, regulate morphogenesis, and ultimately improve crop yield and quality.

6.3 Anti-counterfeiting and information encryption

In the $ScV_xP_{1-x}O_4$:Bi^{3+} solid solution series, samples with different compositions exhibit distinctly different emission spectra under their own optimal wavelengths of excitation, cov-

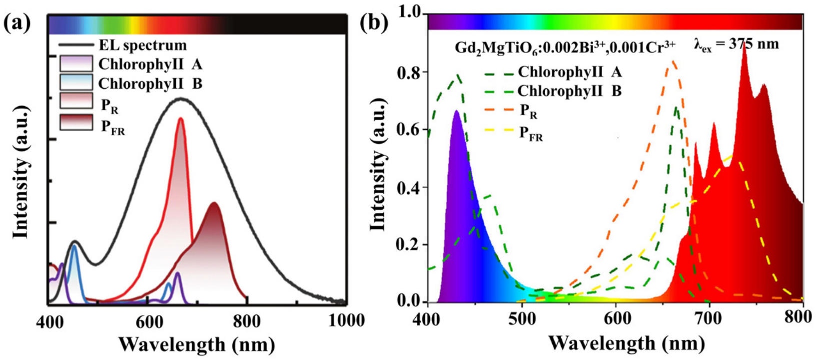

Fig. 15 Comparison of the EL spectra of (a) $Na_2Ca_3Nb_2O_9$:Bi^{3+} (Reproduced with permission from ref. 44, copyright 2022, Wiley-VCH) and (b) Gd_2MgTiO_6:Bi^{3+},Cr^{3+} (reproduced with permission from ref. 93, copyright 2021, Wiley-Blackwell) with the absorption spectra of chlorophyll A, chlorophyll B, red phytochrome (P_R), and far-red phytochrome (P_{FR}).

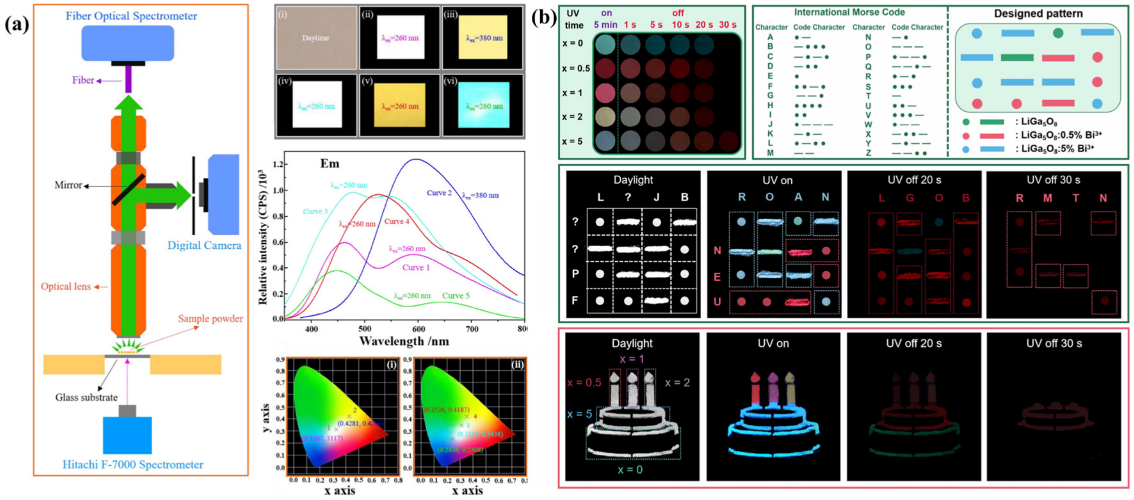

Fig. 16 (a) Digital photographs, emission spectra and CIE coordinates of the blended phosphors excited at different wavelengths. Reproduced with permission from ref. 64, copyright 2019, Royal Society of Chemistry. (b) Application of the $LiGa_5O_8$:Bi^{3+} phosphor in the field of dynamic anti-counterfeiting and information encryption. Reproduced with permission from ref. 94, copyright 2023, American Chemical Society.

ering a broad range from blue to red light. This spectral shift originates from the complex coupling of the internal transitions of Bi^{3+} and the charge-transfer transitions within the crystal structure. Leveraging this emission feature, mixing different $ScV_xP_{1-x}O_4$:Bi^{3+} compositions at specific mass ratios enables excitation-dependent dynamic color tuning, showing application potential of the materials in temporary data storage, information encryption, and anti-counterfeiting (Fig. 16(a)).[64] Yi *et al.*[94] reported that Bi^{3+} ions selectively occupy the $[Li_1O_6]$/$[Ga_1O_6]$ octahedron and $[Ga_2O_4]$ tetrahedron sites in $LiGa_5O_8$, resulting in dual-band emission at 511 nm and 718 nm under 254 nm UV excitation, respectively. The $LiGa_5O_8$:x%Bi^{3+} (x = 0–5.0) phosphors exhibited afterglow luminescence (persistent luminescence, PersL) in various colors, including red, pink, yellow, cyan, and blue. Notably, this is the first time that red PersL is attained with Bi^{3+} single doping. It was also discussed that the PersL originates from oxygen vacancies and Bi_{Li} defects introduced by Bi^{3+} doping. The selective occupation of Bi^{3+} and trap-depth regulation collectively account for the tunable and long-lasting PersL observed in $LiGa_5O_8$:Bi^{3+}. Leveraging the unique optical properties of this phosphor, a multi-level encryption pattern can be constructed based on Morse code (Fig. 16(b)). By utilizing the differences in emission colors and afterglow durations among samples with different doping concentrations, the above design achieved multi-dimensional encryption across both time (with UV on and at 20 s and 30 s after UV cessation) and space (horizontal and vertical directions), as seen in Fig. 16(b). Furthermore, reproducibility and stability are particularly crucial for the practical anti-counterfeiting applications of phosphors. Therefore, the authors conducted three periodic cycling tests and found a stable luminescence color and a consistent afterglow duration.[94] These findings indicate that Bi^{3+}-based red/NIR emitting phosphors hold promising potential for applications in information encryption and anti-counterfeiting technologies.

7 Conclusions and prospects

This review systematically summarizes the recent advances in Bi^{3+}-based red and NIR luminescence, with a focus on the underlying emission mechanism, material design strategy, and application potential. The main conclusions are as follows: the red/NIR emission of Bi^{3+} not only originates from its intrinsic $^3P_1 \rightarrow {}^1S_0$ transition but is also frequently associated with metal-to-metal charge transfer (MMCT), intervalence charge transfer (IVCT), and defect states such as oxygen vacancies. By modulating the host composition and local crystal field environment, broadband emission spanning from ultraviolet to NIR can be achieved. Effective material design strategies include: (1) crystal field engineering: adjusting the Bi–O bond length, coordination polyhedron distortion, and bond covalency through cation substitution can significantly lower the excited state energy levels, leading to a redshift in emission; (2) defect engineering: introducing defects such as oxygen vacancies may promote electron localization and enhance red/NIR emission from Bi^{3+} or facilitate synergistic luminescence involving multiple defect states; (3) energy transfer engineering: leveraging the broad absorption and high efficiency energy transfer of Bi^{3+} to activate other ions capable of red/NIR emission is one of the most effective approaches to achieve efficient long-wavelength luminescence. Furthermore, Bi^{3+}-based red/NIR emitting materials show great potential in optical thermometry, plant cultivation LEDs, anti-counterfeiting, and information encryption. Their tunable luminescence and multi-mode responses (photoluminescence, long-persistent luminescence, mechanoluminescence, and so on) provide a material foundation for designing multifunctional devices.

Despite the significant progress achieved, Bi^{3+}-based red/NIR luminescent materials still face several challenges and opportunities for future development: (1) in-depth analysis of the luminescence mechanism: there is still a debate about luminescent center attribution and the transition process in certain systems, such as those with wide-spectrum NIR emission. More precise identification is required through time-resolved spectroscopy and theoretical calculations; (2) further improvement of luminescence efficiency/thermal stability: the internal quantum efficiency (IQE) and thermal quenching performance of most materials still need enhancement, particularly in the NIR-II region. Strategies such as constructing core–shell structures and introducing energy transfer networks may improve the performance. (3) Exploration of novel host systems: current research mainly focuses on a limited number of systems such as vanadates, tungstates, and aluminates. Future studies should expand to more covalent hosts such as sulfides and halides to achieve greater red shifts and higher luminescence efficiency. Two particularly promising frontiers are Bi^{3+}-doped metal halide perovskites and quantum dots. However, the development of these systems faces significant synthetic challenges, such as high sensitivity to the synthesis atmosphere (inert/reducing), reaction kinetics, and susceptibility to element volatility or non-stoichiometry. Overcoming these synthetic hurdles is a prerequisite for realizing their theoretical luminescence potential. (4) Integration of multifunctional applications: beyond single-function applications, future work should explore the luminescence behavior of Bi^{3+}-based materials under multiple stimuli (light, heat, force, and electricity) and develop integrated applications in multi-mode anti-counterfeiting, smart sensing, and bioimaging. Pioneering efforts should also be directed toward exploiting Bi^{3+} luminescence for bioimaging within the NIR-II window (1000–1700 nm). The superior tissue penetration, reduced scattering, and minimized autofluorescence in the NIR-II window present a compelling case for developing novel Bi^{3+}-activated probes, though challenges in achieving high quantum efficiency and ensuring biocompatibility remain. In summary, Bi^{3+}-based red/NIR phosphors represent an emerging research direction with broad prospects in mechanistic study, material design, and application development. Interdisciplinary collaboration is expected to drive future breakthroughs in performance and application expansion.

Conflicts of interest

There are no conflicts to declare.

Data availability

No X-ray crystallographic or spectroscopic data were utilized in this article. All data supporting the findings of this study are included in the manuscript.

Acknowledgements

This work is supported by the Liaoning Revitalization Talents Program (Grant No. XLYC2403017), the Natural Science Foundation of the Education Department of Liaoning Province (Grant No. JYTMS20231627), the Young Talents Program of Jinzhou (Grant No. JXYC230103), and the Natural Science Foundation of Liaoning province (Grant No. 2025-MSLH-004).

References

1 G. Blasse and A. Bril, Investigations on Bi^{3+}–activated phosphors, *J. Chem. Phys.*, 1968, **48**(1), 217–222.

2 P. Boutinaud, Revisiting the spectroscopy of the Bi^{3+} ion in oxide compounds, *Inorg. Chem.*, 2013, **52**(10), 6028–6038.

3 A. Krasnikov, E. Mihokova, M. Nikl, S. Zazubovich and Y. Zhydachevskyy, Luminescence spectroscopy and origin of luminescence centers in Bi-doped materials, *Crystals*, 2020, **10**(3), 208.

4 A. Yousif and H. C. Swart, Colour tuneable emission from $(Y_{1.995\text{-}x}Ga_x)_2O_3$: Bi^{3+} phosphor prepared by a sol-gel combustion method, *Mater. Lett.*, 2017, **186**, 345–348.

5 S. Yang, X. Xue, Z. Wang, Q. Zhu, X. Wang and J.-G. Li, A novel $SrLaScO_4$: Bi layered perovskite phosphor with broadband green emission: Multi-cationic sites engineering, and application in high color rendering pc-WLED, *Opt. Mater.*, 2024, **152**, 115550.

6 T. Lyu and P. Dorenbos, Charge carrier trapping management in Bi^{3+} and lanthanides doped Li(Sc, Lu)GeO_4 for X-ray imaging, anti-counterfeiting, and force recording, *Appl. Phys. Rev.*, 2024, **11**(1), 011415.

7 W. Geng, X. Zhou, J. Ding and Q. Wu, Unraveling the origin of broadband yellow emission in Bi^{3+}-doped $LuXnGaO_4$ (Xn = Mg, Zn), phosphors, *Dalton Trans.*, 2024, **53**(8), 3589–3598.

8 P. Dang, Q. Zhang, D. Liu, G. Li, H. Lian, M. Shang and J. Lin, Hetero-valent substitution strategy toward orange-red luminescence in Bi^{3+} doped layered perovskite oxide phosphors for high color rendering index white light-emitting diodes, *Chem. Eng. J.*, 2021, **420**, 127640.

9 X. Liu, P. Xiong, H. Liu, S. Wu, Q. Liu, Y. Fu, Z. Ma, M. Peng and Q. Zhang, Origin of D-band emission in a novel Bi^{3+}-doped phosphor $La_3SnGa_5O_{14}$: Bi^{3+}, *J. Mater. Chem. C*, 2021, **9**(10), 3455–3461.

10 K. Chen, P. Gao, Z. Zhang, Y. Ma, Z. Luo, M. S. Molokeevc, Z. Zhou and M. Xia, Zero-thermal-quenching broadband yellow-emitting Bi^{3+}-activated phosphors based on metal to metal charge transfer, *J. Alloys Compd.*, 2024, **986**, 174112.

11 G. Sivakumar, A. T. M. Munthasir, P. Thilagar and S. Natarajan, Towards white light emission through metal-to-metal charge transfer (MMCT) effect in Bi^{3+} activated $Ca_2YTi_{2\text{-}m}Zr_mGa_3O_{12}$ ($0 \leq m \leq 2$) garnets, *Chem. – Eur. J.*, 2025, **31**(17), e202404016.

12 G. Zhou, X. Jiang, J. Zhao, M. Molokeev, Z. Lin, Q. Liu and Z. Xia, Two-dimensional-layered perovskite $ALaTa_2O_7$: Bi^{3+} (A = K and Na) phosphors with versatile structures and tunable photoluminescence, *ACS Appl. Mater. Interfaces*, 2018, **10**(29), 24648–24655.

13 L. Liu, J. Shi, Y. Li, S. Peng, H. Zhong, L. Song and Y. Zhang, Disguise as fluorescent powder: Ultraviolet-B persistent luminescence material without visible light for advanced information encryption and anti-counterfeiting applications, *Chem. Eng. J.*, 2022, **430**, 132884.

14 J. Han, F. Pan, M. S. Molokeev, J. Dai, M. Peng, W. Zhou and J. Wang, Redefinition of crystal structure and Bi^{3+} yellow luminescence with strong near-ultraviolet excitation in La_3BWO_9: Bi^{3+} phosphor for white light-emitting diodes, *ACS Appl. Mater. Interfaces*, 2018, **10**(16), 13660–13668.

15 J. Han, L. Li, M. Peng, B. Huang, F. Pan, F. Kang, L. Li, J. Wang and B. Lei, Toward Bi^{3+} red luminescence with no visible reabsorption through manageable energy interaction and crystal defect modulation in single Bi^{3+}-doped $ZnWO_4$ crystal, *Chem. Mater.*, 2017, **29**(19), 8412–8424.

16 Q. Wei, J. Ding and Y. Wang, A novel tunable extra-broad yellow-emitting nitride phosphor with zero-thermal-quenching property, *Chem. Eng. J.*, 2020, **386**, 124004.

17 H. Cai, H. Chen, H. Zhou, J. Zhao, Z. Song and Q. Liu, Controlling Cr^{3+}/Cr^{4+} concentration in single-phase host toward tailored super-broad near-infrared luminescence for multifunctional applications, *Mater. Today Chem.*, 2021, **22**, 100555.

18 Z.-H. Zheng, B.-M. Liu, Z. Zhou, C.-G. Ma and J. Wang, A simple and generic post-treatment strategy for highly efficient Cr^{3+}-activated broadband NIR emitting phosphors for high-power NIR light sources, *J. Mater. Chem. C*, 2022, **10**(22), 8797–8805.

19 A. C. Van der Steen, J. J. A. Van Hesteren and A. P. Slok, Luminescence of the Bi^{3+} ion in compounds $LiLnO_2$ and $NaLnO_2$ (Ln = Sc, Y, La, Gd, Lu), *J. Electrochem. Soc.*, 1981, **128**(6), 1327–1333.

20 F. S. Ham, Dynamical Jahn-Teller effect in paramagnetic resonance spectra: orbital reduction factors and partial quenching of spin-orbit interaction, *Phys. Rev.*, 1965, **138**(6A), A1727.

21 P. W. M. Jacobs, Alkali halide crystals containing impurity ions with the ns^2 ground-state electronic configuration, *J. Phys. Chem. Solids*, 1991, **52**(1), 35–67.

22 M. Jin, W. Zheng, Z. Gong, P. Huang, R. Li, J. Xu, X. Cheng, W. Zhang and X. Chen, Unraveling the triplet excited-state

dynamics of Bi^{3+} in vacancy-ordered double perovskite Cs_2SnCl_6 nanocrystals, *Nano Res.*, 2022, **15**(7), 6422–6429.

23 P. Boutinaud, Luminescence–structure relationships in solids doped with Bi^{3+}, *Phys. Chem. Chem. Phys.*, 2023, **25**(16), 11027–11054.

24 Z. Zhou, P. Xiong, H. Liu and M. Peng, Ultraviolet-A persistent luminescence of a Bi^{3+}-activated $LiScGeO_4$ material, *Inorg. Chem.*, 2020, **59**(17), 12920–12927.

25 P. W. M. Jacobs, Alkali halide crystals containing impurity ions with the ns^2 ground-state electronic configuration, *J. Phys. Chem. Solids*, 1991, **52**(1), 35–67.

26 J. Ding, Z. An, Z. Wang, Y. Dai, W. Yu, J. Deng, Y. Lai, X. Huang and Q. Wu, Cationic substitution engineering induced Multi-Color light emitting of bismuth in Tantalate used for WLED, *Chem. Eng. J.*, 2023, **477**, 147122.

27 L. Wang, Q. Sun, Q. Liu and J. Shi, Investigation and application of quantitative relationship between sp energy levels of Bi^{3+} ion and host lattice, *J. Solid State Chem.*, 2012, **191**, 142–146.

28 M. Back, J. Ueda, J. Xu, K. Asami, L. Amidani, E. Trave and S. Tanabe, Uncovering the origin of the emitting states in Bi^{3+}-activated $CaMO_3$ (M = Zr, Sn, Ti) perovskites: Metal-to-metal charge transfer versus s-p transitions, *J. Phys. Chem. C*, 2019, **123**(23), 14677–14688.

29 S. Ye, J. Ding and Q. Wu, MMCT-induced high-bright yellow light-emitting phosphor Bi^{3+}-activated Ba_2YGaO_5 used for WLED, *Chem. Eng. J.*, 2022, **428**, 131238.

30 P. Boutinaud and E. Cavalli, Predicting metal-to-metal charge transfer in closed-shell transition metal oxides doped with Bi^{3+} or Pb^{2+}, *Chem. Phys. Lett.*, 2011, **503**(4–6), 239–243.

31 R. H. P. Awater and P. Dorenbos, X-ray induced valence change and vacuum referred binding energies of Bi^{3+} and Bi^{2+} in $Li_2BaP_2O_7$, *J. Phys. Chem. C*, 2016, **120**, 15114–15118.

32 R. H. P. Awater and P. Dorenbos, The Bi^{3+} 6s and 6p electron binding energies in relation to the chemical environment of inorganic compounds, *J. Lumin.*, 2017, **184**, 221–231.

33 P. Boutinaud, On the luminescence of Bi^{3+} pairs in oxidic compounds, *J. Lumin.*, 2018, **197**, 228–232.

34 F. Kang, M. Peng, X. Yang, G. Dong, G. Nie, W. Liang, S. Xua and J. Qiu, Broadly tuning Bi^{3+} emission *via* crystal field modulation in solid solution compounds (Y, Lu, Sc) VO_4: Bi for ultraviolet converted white LEDs, *J. Mater. Chem. C*, 2014, **2**(30), 6068–6076.

35 F. Kang, H. Zhang, L. Wondraczek, X. Yang, Y. Zhang, D.-Y. Lei and M. Peng, Band-gap modulation in single Bi^{3+}-doped yttrium–scandium–niobium vanadates for color tuning over the whole visible spectrum, *Chem. Mater.*, 2016, **28**(8), 2692–2703.

36 P. Dang, D. Liu, X. Yun, G. Li, D. Huang, H. Lian, M. Shang and J. Lin, Ultra-broadband cyan-to-orange emitting Ba_{1+x}, $Sr_{1-x}Ga_4O_8$: Bi^{3+} phosphors: luminescence control and optical temperature sensing, *J. Mater. Chem. C*, 2020, **8**(5), 1598–1607.

37 X. Wang, X. Feng, M. S. Molokeev, H. Zheng, Q. Wang, C. Xu and J.-G. Li, Modulation of Bi^{3+} luminescence from broadband green to broadband deep red in Lu_2WO_6 by Gd^{3+} doping and its applications in high color rendering index white LED and near-infrared LED, *Dalton Trans.*, 2023, **52**(9), 2619–2630.

38 S. Chen, Y. Du, H. Zhao, Y. Yang, Y. Yang, X. Yao, X. Du, J. Wang and R. Yu, Disorder-order transition and metal-to-metal charge transfer induced rare orangish-red emission in Bi^{3+}-activated double perovskite phosphors, *Chem. Eng. J.*, 2024, **502**, 157928.

39 Y. Wei, Z. Gao, X. Yun, H. Yang, Y. Liu and G. Li, Abnormal Bi^{3+}-activated NIR emission in highly symmetric $XAl_{12}O_{19}$ (X = Ba, Sr, Ca) by selective sites occupation, *Chem. Mater.*, 2020, **32**(19), 8747–8753.

40 D. Liu, C. Shan, Y. Yin, B. Wu, J. Gao and L. Tian, $Sr_9La_2W_4O_{24}$: Bi^{3+}/Nd^{3+} phosphors with anomalous red to near-infrared emission (550–1500 nm) and high efficient quantum cutting for multi-application, *Ceram. Int.*, 2025, **51**, 18925–18936.

41 W. Qin, P. Zhang, X. Miao, Y. Yang, S. Li, S. Zhou and W. Liu, Interstitial oxygen defect inducing near-infrared luminescence in $Ca_3La_2W_2O_{12}$ phosphor, *J. Alloys Compd.*, 2025, **1010**, 177970.

42 F. Kang, Y. Zhang, L. Wondraczek, J. Zhu, X. Yang and M. Peng, Processing-dependence and the nature of the blue-shift of Bi^{3+}-related photoemission in $ScVO_4$ at elevated temperatures, *J. Mater. Chem. C*, 2014, **2**(46), 9850–9857.

43 F. Kang, M. Peng, D. Y. Lei and Q. Zhang, Recoverable and unrecoverable Bi^{3+}-related photoemissions induced by thermal expansion and contraction in $LuVO_4$: Bi^{3+} and $ScVO_4$: Bi^{3+} compounds, *Chem. Mater.*, 2016, **28**(21), 7807–7815.

44 H. Zhang, J. Zhang, Y. Su and X. Zhang, Metal to metal charge transfer induced efficient yellow/far–red luminescence in $Na_2Ca_3(Nb, Ta)_2O_9$: Bi^{3+} toward the applications of white–LEDs and plant growth light, *Adv. Opt. Mater.*, 2022, **10**(10), 2200150.

45 Q. Ma, F. Gao, T. Shi, J. Zhang and Y. Zhang, Bi^{3+} full occupancy efficient ultra-wideband emission based on triangle pore structure, *ACS Sustainable Chem. Eng.*, 2024, **12**(14), 5383–5389.

46 Y. Li, S. Gai, H. Zhu, J. Yin, W. Guo, M. S. Molokeev, X. Lu, M. Xia and Z. Zhou, Abnormal Bi^{3+} activated NIR phosphor toward multifunctional LED applications, *Ceram. Int.*, 2023, **49**(23), 39671–39680.

47 J. Sun, H. Liao, W. Li, W. Wang, Y. Wei and G. Li, Broad red emission and luminescence optimization of Bi^{3+} doped $LaSr_2SbO_6$ double perovskite, *Chin. J. Lumin.*, 2025, **46**(9), 1627–1638.

48 Y. Wei, G. Xing, K. Liu, G. Li, P. Dang, S. Liang, M. Liu, Z. Cheng, D. Jin and J. Lin, New strategy for designing orangish-red-emitting phosphor via oxygen-vacancy-induced electronic localization, *Light: Sci. Appl.*, 2019, **8**(1), 15.

49 J. Han, L. Li, M. Peng, B. Huang, F. Pan, F. Kang, L. Li, J. Wang and B. Lei, Toward Bi^{3+} red luminescence with no visible reabsorption through manageable energy interaction and crystal defect modulation in single Bi^{3+}-doped $ZnWO_4$ crystal, *Chem. Mater.*, 2017, **29**(19), 8412–8424.

50 H. Li, J. Cai, R. Pang, G. Liu, S. Zhang, L. Jiang, D. Li, C. Li, J. Feng and H. Zhang, A strategy for developing thermal-quenching-resistant emission and super-long persistent luminescence in $BaGa_2O_4$: Bi^{3+}, *J. Mater. Chem. C*, 2019, **7**(42), 13088–13096.

51 H. Li, R. Pang, G. Liu, W. Sun, D. Li, L. Jiang, S. Zhang, C. Li, J. Feng and H. Zhang, Synthesis and luminescence properties of Bi^{3+}-activated K_2MgGeO_4: a promising high-brightness orange-emitting phosphor for WLEDs conversion, *Inorg. Chem.*, 2018, **57**(19), 12303–12311.

52 T. Hangai, T. Hasegawa, J. Xu, T. Nakanishi, T. Takeda, K. Nakano, K. Hongo, R. Maezono, T. Goto, Y. Sato, A. Okawa and S. Yin, Key role of metal-to-metal charge transfer transition between Mo^{6+} and Bi^{3+} for enhancement in NIR luminescence of Gd_2MoO_6: Bi, Yb nanophosphor, *J. Phys. Chem. C*, 2024, **128**(8), 3351–3360.

53 X. Wang, F. Jahanbazi, J. Wei, C. U. Segre, W. Chen and Y. Mao, Charge transfer-triggered Bi^{3+} near-infrared emission in $Y_2Ti_2O_7$ for dual-mode temperature sensing, *ACS Appl. Mater. Interfaces*, 2022, **14**(32), 36834–36844.

54 H. Li, R. Pang, Y. Luo, H. Wu, S. Zhang, L. Jiang, D. Li, C. Li and H. Zhang, Structural micromodulation on Bi^{3+}-doped $Ba_2Ga_2GeO_7$ phosphor with considerable tunability of the defect-oriented optical properties, *ACS Appl. Electron. Mater.*, 2019, **1**(2), 229–237.

55 D. Liu, X. Yun, P. Dang, H. Lian, M. Shang, G. Li and J. Lin, Yellow/orange-emitting $ABZn_2Ga_2O_7$: Bi^{3+} (A = Ca, Sr; B = Ba, Sr) phosphors: optical temperature sensing and white light-emitting diode applications, *Chem. Mater.*, 2020, **32**(7), 3065–3077.

56 L. Kong, W. Huang, H. Peng, F. Wang, X. Li, W. Yang, Z. Du and B. Zou, Ultrabroadband (Vis-NIR) Emission in Single-Component Double Perovskite Flexible Film with Efficient X-Ray Radioluminescence for Pixel-Level Multispectral Image Fusion and 3D Imaging, *Nano Energy*, 2025, 111415.

57 R. V. Tikale, A. R. Kadam and S. J. Dhoble, Synthesis and luminescence properties of Bi^{3+} activated $Ba_3WO_5Cl_2$ phosphors for plant cultivation applications, *Chem. Data Collect.*, 2022, **40**, 100891.

58 X. Wang, P. Boutinaud, L. Li, J. Cao, P. Xiong, X. Li, H. Luo and M. Peng, Novel persistent and tribo-luminescence from bismuth ion pairs doped strontium gallate, *J. Mater. Chem. C*, 2018, **6**(38), 10367–10375.

59 P. Dang, Q. Zhang, D. Liu, G. Li, H. Lian, M. Shang and J. Lin, Hetero-valent substitution strategy toward orange-red luminescence in Bi^{3+} doped layered perovskite oxide phosphors for high color rendering index white light-emitting diodes, *Chem. Eng. J.*, 2021, **420**, 127640.

60 Y. Wei, C. Heng, H. Yang, P. Dang, M. S. Molokeev, L. Ning and G. Li, Light-induced charge transfer to achieve deep-red emission in $SrSc_2O_4$: Bi toward multiple optical applications, *Chem. Mater.*, 2022, **34**(19), 8831–8839.

61 X. Li, P. Li, Z. Wang, S. Liu, Q. Bao, X. Meng, K. Qiu, Y. Li, Z. Li and Z. Yang, Color-tunable luminescence properties of Bi^{3+} in $Ca_5(BO_3)_3F$ *via* changing site occupation and energy transfer, *Chem. Mater.*, 2017, **29**(20), 8792–8803.

62 N. Yamashita and S. Asano, Luminescence centers of Ca(S: Se): Bi^{3+} and CaO: Bi^{3+} phosphors, *J. Phys. Soc. Jpn.*, 1976, **40**(1), 144–151.

63 P. Liu, Y. Zhang, B. Li, L. Han and Y. Xu, Trap depth engineering in $MgGa_2O_4$: Bi^{3+} for muticolor dynamic anti-counterfeiting, encryption and optical temperature sensing applications, *Chem. Eng. J.*, 2022, **437**, 135389.

64 F. Kang, G. Sun, P. Boutinaud, F. Gao, Z. Wang, J. Lu, Y. Y. Li and S. Xiao, Tuning the Bi^{3+}-photoemission color over the entire visible region by manipulating secondary cations modulation in the $ScV_xP_{1-x}O_4$: $Bi^{3+}(0 \leq x \leq 1)$ solid solution, *J. Mater. Chem. C*, 2019, **7**(32), 9865–9877.

65 C. Wang, Z. Yao, Y. Lei, K. Wu, W. Dai and M. Xu, Photoluminescence tuning of stable $CaYGaO_4$: Bi/Eu *via* compositional modulation and crystallographic site engineering for nUV wLEDs, *Inorg. Chem.*, 2024, **63**(34), 16056–16069.

66 X. Wang, S. Wei, Z. Lyu, D. Sun, T. Tan, L. Zhou, P. Luo, Z. Lu, X. Zhang and H. You, Efficient $Sr_2Ta_2O_7$: Bi^{3+}, $Ln^{3+}(Ln^{3+} = Eu^{3+}, Sm^{3+})$ phosphors for optical thermometry and anti-counterfeiting, *J. Mater. Chem. C*, 2025, **13**(11), 5823–5834.

67 J. Li, S. Zhang, H. Luo, Z. Mu, Z. Li, Q. Du, J. Feng and F. Wu, Efficient near ultraviolet to near infrared downconversion photoluminescence of La_2GeO_5: Bi^{3+}, Nd^{3+} phosphor for silicon-based solar cells, *Opt. Mater.*, 2018, **85**, 523–530.

68 H. Arfin, J. Kaur, T. Sheikh, A. P. S. Chakraborty and A. P. A. Nag, Bi^{3+}–Er^{3+} and Bi^{3+}–Yb^{3+} codoped $Cs_2AgInCl_6$ double perovskite near–infrared emitters, *Angew. Chem., Int. Ed.*, 2020, **59**(28), 11307–11311.

69 X.-Y. Huang, X.-H. Ji and Q.-Y. Zhang, Broadband downconversion of ultraviolet light to near–infrared emission in Bi^{3+}–Yb^{3+}–codoped Y_2O_3 phosphors, *J. Am. Ceram. Soc.*, 2011, **94**(3), 833–837.

70 R. V. Yadav, R. S. Yadav, A. Bahadur, A. K. Singh and S. B. Rai, Enhanced quantum cutting *via* Li^+ doping from a Bi^{3+}/Yb^{3+}-codoped gadolinium tungstate phosphor, *Inorg. Chem.*, 2016, **55**(21), 10928–10935.

71 R. A. Talewar, S. K. Mahamuda, A. S. Rao and S. V. Moharil, Intense infrared emission of Er^{3+} in ZnB_2O_4 phosphors from energy transfer of Bi^{3+} by broadband UV excitation, *J. Lumin.*, 2022, **244**, 118706.

72 D. Huang, P. Dang, H. Lian, Q. Zeng and J. Lin, Luminescence and energy-transfer properties in Bi^{3+}/Mn^{4+}-codoped Ba_2GdNbO_6 double-perovskite phosphors for white-light-emitting diodes, *Inorg. Chem.*, 2019, **58**(22), 15507–15519.

73 Y.-L. Yang, X.-C. Yang, J.-Y. Yuan, T. Li, Y.-T. Fan, L. Wang, Z. Deng, Q.-L. Li, D.-Y. Wan, J.-T. Zhao and Z.-J. Zhang,

Time–resolved bright red to cyan color tunable mechanoluminescence from CaZnOS: Bi^{3+}, Mn^{2+} for anti–counterfeiting device and stress sensor, *Adv. Opt. Mater.*, 2021, **9**(16), 2100668.

74 X. Sun, J. Li, K. Feng, R. Zheng and H. Yuan, Luminescence characteristics of Bi^{3+}, Cr^{3+} and Bi^{3+}/Cr^{3+} activated $Sr_3Y_2Ge_3O_{12}$ phosphors, *J. Lumin.*, 2022, **248**, 118984.

75 K. Li, X. Chen, Y. Feng, Y. Fu, P. Chen, J. Lu, B. Wei, L. Zheng, J. Tao and Q. Liu, Luminescence improvement of $Gd_3Ga_5O_{12}$: Cr^{3+}, Bi^{3+} NIR phosphor with superior thermal stability for plant cultivation, *J. Alloys Compd.*, 2024, **979**, 173582.

76 S. Wu, P. Xiong, Q. Liu, Y. Xiao, Y. Sun, E. Song and Y. Chen, Self–activated tungstate phosphor for near–infrared light–emitting diodes, *Adv. Opt. Mater.*, 2022, **10**(23), 2201718.

77 X. Xue, S. Yang, W. Liu, L. Dong, Q. Zhu, X. Wang and J.-G. Li, $NaLaCaWO_6$ double perovskite: Structure analysis, efficient Bi^{3+} to Eu^{3+} energy transfer and favourable visual optical thermometry, *J. Mol. Struct.*, 2025, **1333**, 141797.

78 K. Li, H. Lian, M. Shang and J. Lin, A novel greenish yellow-orange red $Ba_3Y_4O_9$: Bi^{3+}, Eu^{3+} phosphor with efficient energy transfer for UV-LEDs, *Dalton Trans.*, 2015, **44**(47), 20542–20550.

79 P. Dang, S. Liang, G. Li, Y. Wei, Z. Cheng, H. Lian, M. Shang, J. Seong and J. Lin, Controllable optical tuning and improvement in Li^+, Eu^{3+}-codoped $BaSc_2O_4$: Bi^{3+} based on energy transfer and charge compensation, *J. Mater. Chem. C*, 2018, **6**(24), 6449–6459.

80 P. Dang, S. Liang, G. Li, H. Lian, M. Shang and J. Lin, Broad color tuning of Bi^{3+}/Eu^{3+}-doped $(Ba, Sr)_3Sc_4O_9$ solid solution compounds *via* crystal field modulation and energy transfer, *J. Mater. Chem. C*, 2018, **6**(37), 9990–9999.

81 F. Kang, Y. Zhang and M. Peng, Controlling the energy transfer *via* multi luminescent centers to achieve white light/tunable emissions in a single-phased X2-type Y_2SiO_5: Eu^{3+}, Bi^{3+} phosphor for ultraviolet converted LEDs, *Inorg. Chem.*, 2015, **54**(4), 1462–1473.

82 O. A. Lipina, A. V. Chvanova, L. L. Surat, Y. V. Baklanova, A. Y. Chufarov, A. P. Tyutyunnik and V. G. Zubkov, Color-tunable luminescence and temperature sensing properties of Bi^{3+}/Sm^{3+} or Bi^{3+}/Eu^{3+} codoped $Ba_2Gd_2Ge_4O_{13}$ phosphors, *Dalton Trans.*, 2024, **53**(18), 7985–7995.

83 J. Li, S. Zhang, H. Luo, Z. Mu, Z. Li, Q. Du, J. Feng and F. Wu, Efficient near ultraviolet to near infrared downconversion photoluminescence of La_2GeO_5: Bi^{3+}, Nd^{3+} phosphor for silicon-based solar cells, *Opt. Mater.*, 2018, **85**, 523–530.

84 Q. Xiao, J. Meng and J. Qiu, Near-infrared luminescence enhancing by co-doping Bi^{3+} in YVO_4: Nd^{3+}, *J. Alloys Compd.*, 2013, **574**, 600–603.

85 Z. Zhou, Y. Zhong, M. Xia, N. Zhou, B. Lei, J. Wang and F. Wu, Tunable dual emission of $Ca_3Al_4ZnO_{10}$: Bi^{3+}, Mn^{4+} *via* energy transfer for indoor plant growth lighting, *J. Mater. Chem. C*, 2018, **6**(33), 8914–8922.

86 B. Li, Y. Li, B. Cao, C. Yang, R. Ma, C. Deng and W. Huang, Mn^{4+} co-doped double perovskite $CaSrLaSbO_6$: Bi^{3+} phosphors with multiple luminescent centers for optical temperature sensing and indoor plant cultivation films, *Colloids Surf., A*, 2025, **713**, 136542.

87 Y.-L. Yang, J.-Y. Yuan, Y.-T. Fan, D.-Y. Wan, Q.-L. Li, J.-T. Zhao and Z.-J. Zhang, Efficient energy transfer from Bi^{3+} to Mn^{2+} in CaZnOS for WLED application, *Dalton Trans.*, 2021, **50**(32), 11130–11136.

88 L. Dong, L. Zhang, Y. Jia, B. Shao, S. Zhao and H. You, Luminescence properties and energy transfer of novel Bi^{3+} and Mn^{2+}-co-activated $Y_3Ga_5O_{12}$ single-component white light-emitting phosphor, *J. Mater. Chem. C*, 2020, **8**(35), 12231–12239.

89 M. Feizbakhsh, A. Doosti and A. Keshavarzi, Energy transfer from Bi^{3+} to Mn^{2+} doped in oxyfluoride glass and transparent glass-ceramics containing $KMgF_3$, *J. Solid State Chem.*, 2022, **308**, 122938.

90 X. Lv, R. Xiao, J. Liu, C. Yang, Y. Xin and N. Guo, Recent progress on modulating luminescence thermal quenching properties of Bi^{3+}-activated phosphors, *Inorg. Chem. Front.*, 2024, **11**(6), 1668–1682.

91 N. C. George, J. Brgoch, A. J. Pell, C. Cozzan, A. Jaffe, G. Dantelle, A. Llobet, G. Pintacuda, R. Seshadri and B. F. Chmelka, Correlating local compositions and structures with the macroscopic optical properties of Ce^{3+}-doped $CaSc_2O_4$, an efficient green-emitting phosphor, *Chem. Mater.*, 2017, **29**(8), 3538–3546.

92 K. A. Denault, J. Brgoch, S. D. Kloß, M. W. Gaultois, J. Siewenie, K. Page and R. Seshadri, Average and local structure, Debye temperature, and structural rigidity in some oxide compounds related to phosphor hosts, *ACS Appl. Mater. Interfaces*, 2015, **7**(13), 7264–7272.

93 P. Gao, Z. Zhou, P. Dong, Q. Li, H. Li, J. Wang, Z. Zhou and M. Xia, Tuning the luminescence properties of blue and far–red dual emitting Gd_2MgTiO_6: Bi^{3+}, Cr^{3+} phosphor for LED plant lamp, *J. Am. Ceram. Soc.*, 2021, **104**(12), 6444–6454.

94 Z. Yi, P. Liu, X. Liu and Y. Xu, Prolonged red persistent luminescence in Bi^{3+} single-doped $LiGa_5O_8$: regulating traps by site selective occupation, *Inorg. Chem.*, 2023, **62**(48), 19542–19551.